Is the molecular KS relationship universal down to low metallicities?

David J. Whitworth [1]★ Rowan J. Smith [1]★ Robin Tress [2] Scott T. Kay [1] Simon C. O. Glover [2]
Mattia C. Sormani [2] and Ralf S. Klessen [2,3]

[1]*Jodrell Bank Centre for Astrophysics, Department of Physics and Astronomy, University of Manchester, Oxford Road, Manchester M13 9PL, UK*
[2]*Universitat Heidelberg, Zentrum fur Astronomie, Institut fur Theoretische Astrophysik, Albert-Ueberle-Str. 2, D-69120 Heidelberg, Germany*
[3]*Universität Heidelberg, Interdisziplinäres Zentrum für Wissenschaftliches Rechnen, Im Neuenheimer Feld 205, D-69120 Heidelberg, Germany*

ABSTRACT

In recent years, it has been speculated that in extreme low-metallicity galactic environments, stars form in regions that lack H_2. In this paper, we investigate how changing the metallicity and ultraviolet (UV) field strength of a galaxy affects the star formation within, and the molecular gas Kennicutt–Schmidt (KS) relation. Using extremely high-resolution AREPO simulations of isolated dwarf galaxies, we independently vary the metallicity and UV field to between 1 per cent and 10 per cent solar neighbourhood values. We include a non-equilibrium, time-dependent chemical network to model the molecular composition of the interstellar medium and include the effects of gas shielding from an ambient UV field. Crucially, our simulations directly model the gravitational collapse of gas into star-forming clumps and cores and their subsequent accretion using sink particles. In this first publication, we find that reducing the metallicity and UV field by a factor of 10 has no effect on star formation and minimal effect on the cold, dense star-forming gas. The cold gas depletion times are almost an order of magnitude longer than the molecular gas depletion time due to the presence of star formation in HI dominated cold gas. We study the H_2 KS relationship that arises naturally within the simulations and find a near-linear power-law index of $N = 1.09 \pm 0.014$ in our fiducial 10 per cent solar metallicity model. As the metallicity and UV field are reduced, this becomes moderately steeper, with a slope of $N = 1.24 \pm 0.022$ for our 1 per cent solar metallicity and 1 per cent solar UV field model.

Key words: hydrodynamics – stars: formation – ISM: clouds – ISM: structure – galaxies: ISM.

1 INTRODUCTION

Dwarf galaxies are the most numerous type of galaxies in the universe and are important building blocks to assemble larger galaxies. They have low surface brightness, shallow gravitational potential wells, and relatively low star formation rates (SFRs) compared to larger galaxies. Due to their shallow gravitational potential wells, they react sensitively to external and internal processes such as feedback by supernovae (SNe) and cosmic ray ionization and are therefore ideal objects to study galaxy evolution. With dwarf galaxies showing lower metallicities (Z), they are useful test laboratories for studying how the interstellar medium (ISM) responds to varying chemical and physical processes, which are hard to model accurately for Milky Way-like galaxies.

Dwarfs can be thought of as analogous to high redshift galaxies. Understanding how star formation behaves in these extreme conditions will help us to understand how the first galaxies and stars formed in the early, post-reionization, universe. Dwarf galaxies are also progenitors to larger galaxies through mergers, so an understanding of dwarfs can lead to a greater understanding of larger galaxies and their evolution. For example, Shi et al. (2014) show that in nearby extremely metal poor galaxies (XMPs), star formation is inefficient.

These XMPs are our closest analogous galaxies to high-redshift galaxies and provide the best observational results to draw from.

At extremely low metallicities, H_2 formation is inefficient due to the reduced availability of the dust grain surfaces that allow the HI to H_2 reaction to occur (Palla, Salpeter & Stahler 1983; Omukai, Hosokawa & Yoshida 2010). This has implications for our understanding of how stars form within these galaxies. Observations of star-forming spiral galaxies from multiple surveys [e.g. THINGS (Walter et al. 2008), SINGS (Kennicutt et al. 2003), GALEX NGS (Gil de Paz et al. 2007), the HERACLES (Leroy et al. 2008) or BIMA-SONG (Helfer et al. 2003) CO surveys, and the spatially resolved PHANGS survey (Pessa et al. 2021)] have shown that the star formation surface density (Σ_{SFR}) is strongly correlated with molecular hydrogen surface density (Σ_{H_2}), and only loosely correlated to atomic hydrogen or total gas surface density. The seminal work by Bigiel et al. (2008), for example, found a molecular gas Kennicutt–Schmidt (KS) relationship ($\Sigma_{SFR} \propto \Sigma_{H_2}^N$) with an exponent of $N = 1.0 \pm 0.2$ in spiral galaxies where the total gas relation varies dramatically from a low of $N = 1.1$ to $N = 2.7$.

Such work is now being extended to the low-metallicity regime. de los Reyes & Kennicutt (2019) looked at the relation between H_2 and star formation in a large sample of 307 quiescent spiral, dwarf, or low surface brightness galaxies to revise the KS relationship. They find a revised KS relationship using HI + H_2 surface density of $N = 1.4 \pm 0.07$ for spirals, which drops to $N = 1.26 \pm 0.08$ for dwarfs. When looking only at H_2 in spirals, this becomes a sub-linear relationship with an exponent of $N = 0.67 \pm 0.05$, significantly shallower

★ E-mail: david.whitworth@manchester.ac.uk (DJW);
rowan.smith@manchester.ac.uk (RJS)

than in the higher metallicity spirals of Bigiel et al. ([2008](#)). One of the problems with finding the molecular KS relationship for dwarf galaxies is the difficulty in detecting H_2 within them; Roychowdhury et al. ([2015](#)) and Filho et al. ([2016](#)) both look at the dominant HI component in CO-dark dwarf galaxies and note that it is not a good tracer for H_2 or star formation and the respective KS relationship.

However, characterizing such relationships is always challenging in low-metallicity systems due to the necessity of using an assumed X_{CO} conversion factor (Bolatto, Wolfire & Leroy [2013](#)) to convert from CO emission to the actual molecular gas mass. Detecting CO emission from faint sources and constraining the X_{CO} factor is much harder in such systems. For these reasons, numerical simulations have an important role to play in characterizing star formation and its relation to molecular gas in dwarf systems.

The link between molecular gas and star formation has been a topic of some discussion in the literature. Krumholz ([2012](#)) proposed that star formation will occur in the cold atomic phase of the ISM in galaxies and clouds with metallicities of a few per cent of $Z_\odot$ or lower. Similarly, Glover & Clark ([2012a](#), [b](#)), and Hu, Sternberg & van Dishoeck ([2021](#)) propose that molecular gas and star formation coincide in metal-rich galaxies due to gravitational instability creating favourable conditions for the formation of both and not because of a causal connection between H_2 and star formation. They suggest that at low metallicities, the link between H_2 and star formation may break down. However, these works were not full galaxy simulations, and to fully understand these ideas, an analysis on galactic scales is needed.

A related issue is the effect of varying the ultraviolet (UV) field strength (G_0) upon star formation. Hu et al. ([2016](#), [2017](#)) performed simulations at a fixed metallicity of $Z = 0.1$ solar and found that modifying the UV field had little impact upon the SFR surface density. On the other hand, Ostriker, McKee & Leroy ([2010](#)) find a linear connection between SFR surface density and G_0 in gravitationally bound clouds.

In this work, we aim to investigate how changing the metallicity and average UV field impacts upon the SFR and resulting molecular gas KS relations in a set of high-resolution isolated dwarf galaxy simulations. We select our metallicity regime such that we include dwarfs with $Z = 0.01$ solar where Krumholz ([2012](#)) suggested that star formation becomes associated with cold atomic gas. The models include hydrodynamics, self-gravity, non-equilibrium heating, cooling and chemistry, a new chemical network suited to diffuse gas, shielding, and SNe feedback. Crucially, our simulations directly model the gravitational collapse of gas into star-forming clumps and cores and their subsequent accretion using sink particles (Bate, Bonnell & Price [1995](#); Tress et al. [2020](#)). This is in contrast to more commonly adopted stochastic star formation models that randomly create stars from gas above a given density, given an SFR per free-fall time. This enables us to directly link the mass involved in star formation to the energetic properties of the region of the ISM in which it forms.

The paper is structured as follows. In Section 2, we lay out the numerical models used. In Section 3, we detail the results from the simulations. Section 4 discusses the implications of the results and caveats. In Section 5, we provide a summary of our work.

2 METHODS

2.1 Modelling

The simulations in this work are performed using the quasi-Lagrangian moving mesh code AREPO (Springel [2010](#)). AREPO solves the hydrodynamic equations on a 3D moving mesh with a second-order Godunov scheme that uses an exact Riemann solver using Heuns method, as described in Pakmor et al. ([2016](#)).

To do this, it uses a set of discrete points to generate a Delaunay triangulation, which is then used to construct a 3D unstructured Voronoi mesh. The code allows the points to move with the local velocity of the gas, reconstructing the mesh after each time-step. This allows the cells to move, adapt, and continuously change while the mass in each cell remains approximately constant. It also means that the fluid density has a strong influence on the resolution of the code. At higher densities, the cells of the mesh are smaller, giving finer resolution; at lower densities, like the edge of the simulation, where fine resolution is not needed, the cells are much larger.

AREPO uses a Barnes-Hut tree-based approach based on that of GADGET-3 (Springel [2005](#)) to calculate the gravitational potential and can consider multiple cell/particles types. In our simulations, we include both dark matter particles to model the galaxy halo, gas cells that interact hydrodynamically, collisionless star particles, and sink particles representing regions of ongoing star formation. In the following sections, we discuss in more detail our custom ISM physics modules, but for a more detailed discussion of the AREPO code in general, see Springel ([2010](#)) and Weinberger, Springel & Pakmor ([2019](#)).

2.2 Chemical network

In our simulations, we use a slightly modified version of the chemical network presented in Gong, Ostriker & Wolfire ([2017](#)). This network (hereafter the [GOW17](#) network) has been benchmarked against a highly accurate photo-dissociation region (PDR) code across a wide range of temperatures, pressures, and metallicities (Gong et al. [2017](#)). It accurately reproduces the CO abundances in a 1D equilibrium model but in high-density regions may over-produce CO. Our implementation is a non-equilibrium, time-dependent 3D version of the above that contains several additional reactions that are unimportant in PDR conditions but that make the network more robust when dealing with hot, shocked gas. Full details of these modifications can be found in Hunter et al. ([2021](#)).

The self-shielding by CO of the non-ionizing UV interstellar radiation field and the H_2 self-shielding are modelled using the TreeCol algorithm developed by Clark, Glover & Klessen ([2012](#)), with a shielding length of 30 pc. The heating and cooling of the gas are computed simultaneously with its chemical evolution. We use the new molecular and atomic cooling functions from Clark et al. ([2019](#)). This improved treatment of gas cooling at high temperatures ($T \gg 10^4$ K) is key for modelling the effects of SNe feedback in our simulations. Within the network, we trace nine individual non-equilibrium species: H_2, H^+, C^+, CH_x, OH_x, CO, HCO^+, He^+, and Si^+ plus a further eight, which are derived from conservation laws or the assumption of chemical equilibrium: free electrons, H, H_3^+, C, O, O^+ He, and Si. The pseudo-species CH_x and OH_x represent CH, CH_2, CH^+, CH_2^+ etc. in the first case, and OH, OH^+, H_2O^+, H_2O etc. in the second case.

180.0ptIn our simulations, we vary the metallicity with respect to the solar reference value by decreasing the carbon abundance, oxygen abundance, and dust-to-gas ratio in line with the reduction in Z. For simplicity, we assume a linear scaling between the dust-to-gas ratio and Z, though in reality observations hint at a steeper relation at low Z (see e.g. Rémy-Ruyer et al. [2014](#)). Similarly, we scale the magnitude of the cosmic ray ionization rate of atomic hydrogen ($\zeta_H(s^{-1})$) based on the magnitude of our chosen UV field strength (G_0), under the assumption that both scale linearly with the SFR. For our fiducial model, we consider all variables to be 10 per cent of

Table 1. Values used for metallicity (Z), dust-to-gas ratio (relative to the value in solar metallicity gas), cosmic ionization rate ($\zeta_H(s^{-1})$), and UV-field strength [G_0 (Habing units)] in the initial conditions for each of the four simulations.

Model name	$Z(Z_\odot)$	Dust to gas	ζ_H (s^{-1})	G_0 (Habing units)
Z.10 G.10	0.10	0.10	3.0×10^{-18}	0.17
Z.10 G.01	0.10	0.10	3.0×10^{-19}	0.017
Z.01 G.10	0.01	0.01	3.0×10^{-18}	0.17
Z.01 G.01	0.01	0.01	3.0×10^{-19}	0.017

Table 2. Sink particle parameters used across all four simulations. ρ_c is the sink density threshold, r_{SF} is the accretion radius, ϵ_{SF} is the star formation efficiency, and r_{SNe} is the radius of scatter for SNe around the sink particle.

ρ_c (g cm^{-3})	2.4×10^{-20}
n (cm^{-3})	1e4
r_{acc} (pc)	1.75
Softening length (pc)	2.0
ϵ_{SF}	0.1
r_{SNe} (pc)	5

solar ($Z = 0.10\,Z_\odot$, $G_0 = 0.17$). We then run three more simulations with the variables as seen in Table 1.

2.3 Sink particles

For stars to form, gas within the ISM must undergo gravitational collapse to protostellar densities. Even at dwarf galaxy scales, it is computationally unfeasible to simulate the entirety of the star formation process. In order to proceed, we adopt the use of collisionless sink particles (sinks), a technique that has been widely adopted in computational studies of star formation (Bate et al. 1995; Federrath et al. 2010). Here, we replace the densest collapsing and gravitationally bound regions of a molecular cloud with a sink particle that can undergo future accretion. Our method is the same as that of Tress et al. (2020), who integrate sink particles in a galactic scale simulation successfully.

Sinks form when, within a given accretion radius, r_{acc}, a region with density greater than a defined threshold ρ_c satisfies the following criteria:

(i) The gas flow must converge. To define this, both the velocity divergence and the divergence of the acceleration must be negative.

(ii) The collapsing region must be centred on a local potential minimum.

(iii) The region cannot be within the accretion radius of any other sink particles and should not move within the accretion radius in a time less than the local free-fall time.

(iv) The region must be gravitationally bound. To do this, it must satisfy the conditions: $U > 2(E_k + E_{th})$, where $U = GM^2/r_{acc}$ is the gravitational energy of the region within the accretion radius, $E_k = 1/2\Sigma_i m_i \Delta v_i^2$ is the total kinetic energy of the gas within the accretion radius where m_i and Δv_i are the mass and velocity dispersion within cell i and we sum overall cells within the accretion radius, and $E_{th} = \Sigma_i m_i e_{th,\,i}$ is the total internal energy of the region where $e_{th,\,i}$ is the specific thermal energy of cell i.

These ensure that a sink is formed only if the gas is truly self-gravitating and collapsing.

When a gas cell satisfies these conditions, it is converted into a sink particle that is allowed to accrete mass. It can do this if the gas

within r_{acc} is above the density threshold and gravitationally bound to the sink particle. The amount of mass accreted on to the sink from the cell is calculated by:

$$\Delta m = (\rho_{cell} - \rho_c)V_{cell}, \qquad (1)$$

where ρ_{cell} is the initial gas density of the cell and V_{cell} is the volume. We limit the accreted mass to no more than 90 per cent of the initial mass of the cell. Once the mass has been removed from the cell, the new density of the cell is the threshold density ρ_c, and any other values that depend on the mass are updated as necessary. If the gas cell lies within the accretion radii of multiple sinks, the accreted mass is given to the sink with which it is most strongly bound. We set a maximum stellar mass threshold of each sink to 200 $M_\odot$. Above this, accretion is turned off, instead allowing another sink to form. In this way, our sinks always resemble small stellar sub-clusters, and any large star-forming region will contain multiple sinks.

The time-stepping used by AREPO allows gas cells to be active on different time-steps to the sink particles. Accretion occurs only when a gas cell and the sink particle it is bound to are both active. So that accretion is not missed from cells that spend a short time within r_{acc}, the time-step on which the sinks are evolved is kept equal to the shortest gas cell time-step.

To ensure that collapse and any fragmentation that might occur are properly resolved, we ensure that the local Jeans length (JL) is resolved by at least eight resolution elements (Truelove et al. 1997; Federrath et al. 2011). However, the JL in the coldest and densest regions of a molecular cloud can become prohibitively small at high densities. To overcome this, a density threshold for refinement is implemented, $\rho_{lim} = 2.4 \times 10^{-20}$ g cm^{-3}, which also defines the sink creation density, i.e. $\rho_c = \rho_{lim}$. At densities above ρ_{lim}, we no longer refine the grid; however, any unaccreted gas at these densities is still able act hydrodynamically with its environment and may continue to increase in density. This strikes a balance between computational efficiency and high resolution within dense regions.

The gravitational softening length for the collisionless sink particles is 2 pc as in Hu et al. (2016) to allow a comparison (but with higher resolution in our gas cells). Our sinks should therefore be thought of as small sub-clusters of stars, rather than as individual stellar systems. Other studies use a more stochastic approach that creates stars of a given mass in the densest regions of the ISM, given an efficiency per free-fall time. Our approach ties the star formation directly to the cold dense gas in the ISM allowing us to causally connect the sink mass to the material that is gravitationally bound. Table 2 summarises the parameters used for the sink particles.

2.4 Feedback

By using the chemical model discussed above with the cooling and self-shielding properties of molecular gas, we are able to form molecular clouds. However, such clouds have a finite lifetime. Galactic shear has been shown to be too inefficient a disruptive process to produce realistic cloud lifetimes and masses (Jeffreson & Kruijssen 2018), and so stellar feedback must be included.

The sinks are associated with a discrete stellar population based on the formalism of Sormani et al. (2017). Using an initial mass function (IMF), a set of discrete mass bins is populated via a Poisson distribution with a carefully chosen mean for each bin. This ensures that the mass distribution of stars within a sink particle follows the chosen IMF even if the sink is too small to fully sample the IMF. For each star that is more massive that 8 $M_\odot$ formed in this way, an SNe explosion is generated at the end of the star's lifetime, according to its mass in table 25.6 of Maeder (2009).

As sink particles represent groups of stars, we do not assume that the related SNe occur directly at the location of the sink. To position them, we randomly sample a Gaussian distribution centred on the sink's location with a standard deviation $r_{SNe} = 5$ pc, based on an average cloud size of 10pc.

We assume an star formation (SF) efficiency in the sink of $\epsilon_{SF} = 0.1$. Our choice of ϵ_{SF} is motivated by the fact that even at our sink creation density ($\rho_c = 2.4 \times 10^{-20}$ g cm^{-3}, $n = 10^4$ cm^{-3}), star formation is still inefficient (Krumholz & McKee 2005; Evans et al. 2009). It is also consistent with the observed range of star formation efficiencies in dense molecular gas (Krumholz, Dekel & McKee 2012; Evans, Heiderman & Vutisalchavakul 2014; Heyer et al. 2016; Jeffreson et al. 2021). Our sink particle model does not allow us to directly trace the composition of the sink, and so we make the assumption based on our ϵ_{SF} that 90 per cent of the mass of the sink is in the form of gas, which is gradually returned to the ISM through our feedback mechanisms explained below. The remainder of the mass in the sink is considered to be locked in stars.

After the last SNe tied to a sink particle has occurred, the sink has the same mass as the stellar component alone. When this happens, it gets turned into a collisionless *N*-body star particle. However, some sinks will not accrete enough mass to form a massive star. This means that the gas in the sink will not be returned to the ISM from an SNe. To account for this, after a period of 10 Myr, if a sink has not formed a massive star, then the star is turned into a star particle and the remaining gas mass is returned to the ISM by uniformly adding the gas mass to all gas cells surrounding the sink out to 100 pc.

The energy injection from the supernova is modelled from a modified version of an algorithm originally implemented in AREPO by Bubel (2015). We calculate the radius of the supernova remnant (R_{sr}) at the end of its Sedov–Taylor phase assuming an SNe energy of 10^{51} erg and measure a local mean density of $\bar{n}$. This is then compared to the injection region (R_{inj}), a sphere around the SNe that contains 32 Voronoi cells. If $R_{sr} > R_{inj}$, then we inject 10^{51}erg into the injection region as thermal energy and have the gas become fully ionized. When this is not the case and the SN remnant is unresolved, then the local density is considered too high for thermal injection, as it would radiate away too quickly to generate strong shocks or deposit the correct amount of kinetic energy into the surrounding ISM. In response to this, the code directly injects the correct terminal momentum instead, without changing the temperature or ionization state of these regions. The injection radius is kept small so that we minimize when we inject momentum into the ISM instead of thermal energy. This method for injecting SNe into simulations has been previously used successfully by a number of other authors (Hopkins et al. 2014; Kimm & Cen 2014; Simpson et al. 2015; Walch et al. 2015; Kim & Ostriker 2017).

Due to the relatively low stellar mass of a dwarf galaxy and the low expected rate of Type Ia SNe in such a small population, we include only Type II SNe. Naturally, there are other forms of feedback that are associated with star formation and dispersing giant molecular clouds (GMCs), e.g. stellar winds and radiation from young stars and photoionization. These are important as they affect the ISM before SNe feedback commences (Dale et al. 2014; Inutsuka et al. 2015; Gatto et al. 2017; Rahner et al. 2019; Chevance et al. 2022). However, to include all forms of feedback remains computationally difficult, and as such we leave this for future work. Excluding photoionization will likely lead to an underestimation of H$^+$ and overestimation of H, and so we place a caveat on this. Jeffreson et al. (2021) include HII region feedback mechanisms in a Milky Way-like galaxy and see no effect on star formation compared to runs with only SNe feedback but do note a change in the ISM and cloud characteristics.

Table 3. Parameters for the different galactic components.

	Mass (M$_\odot$)	Scale length (kpc)	h_z (kpc)
DM halo	2.00×10^{10}	7.62	–
Gas disc	8.00×10^7	0.82	0.35

2.5 Initial conditions

We set up the dwarf galaxy as a stable disc in isolation. It consists of two initial components: a dark matter halo and a gaseous disc, Fig. 1. Stars are not initially included but are created from sinks created during the initial burst before the galaxy reaches the steady-state period, which we use for analysis. The steady-state period has stars present throughout its entirety. The size parameters are summarized in Table 3.

The dark matter halo uses a spheroidal Hernquist (1990) profile following:

$$\rho_{sph}(r) = \frac{M_{sph}}{2\pi} \frac{a}{r(r+a)^3}, \qquad (2)$$

where r is the radius of the sphere, a is the scale length of the halo, and M_{sph} is the mass of the halo.

The gaseous disc component follows a double exponential density profile:

$$\rho_{disc}(R, z) = \frac{M_{disc}}{2\pi h_z H_R^2} \text{sech}^2 \left(\frac{z}{2h_z} \right) \exp \left(-\frac{R}{h_R} \right), \qquad (3)$$

where R is the disc radius and z is its height, h_z and h_R are the scale height (0.35 kpc) and scale length (0.82 kpc) of the disc, respectively.

The initial conditions are generated using the method from Springel, Di Matteo & Hernquist (2005). The values have been chosen to be broadly comparable to Hu et al. (2016). The total baryonic mass is 8.00×10^7 M$_\odot$, slightly higher that Hu et al. (2016). Metallicity, the dust-to-gas ratio, cosmic ray ionization rate, and the UV field are all set to 10 per cent solar for the fiducial simulation. It is generally assumed that the relation between the SFR surface density and G_0 is linear (Ostriker et al. 2010), but to test this, we vary the above parameters between 1 per cent and 10 per cent of the solar neighbourhood value. Table 1 shows the values used for the four simulations. The initial temperature of the gas is set to $T = 10^4$ K, and the composition is initially fully atomic.

2.6 Resolution

Within the simulations, we set a base mass resolution for the gas cells of 100 M$_\odot$, for the first 300 Myr and then set it to 50 M$_\odot$ for the remainder of the simulation. The code will refine/de-refine a cell to keep them within a factor of 2 of this mass. However, on top of this, we add a more stringent requirement that the local JL is resolved by at least eight resolution elements. Due to the Jeans refinement, in the densest regions of the ISM, we resolve to below solar masses as shown in Fig. 2. For a total gas number density of $n = 100$ cm^{-3}, we have a cell radius (r_{eff}) of 0.50 pc, and at $n = 10^4$ cm^{-3}, r_{eff} is 0.16 pc (Fig. 2). These high spatial resolutions are essential for accurately capturing the fragmentation behaviour of the dense gas clouds where our sink particles will form (Truelove et al. 1997).

As AREPO uses an adaptive mesh, the gas cells range in size and mass and so we cannot use a unique gravitational softening length. We therefore apply adaptive softening to the gas cells, with a softening length that varies with the cell radius. For the dark matter, we use a fixed softening length of 640 pc.
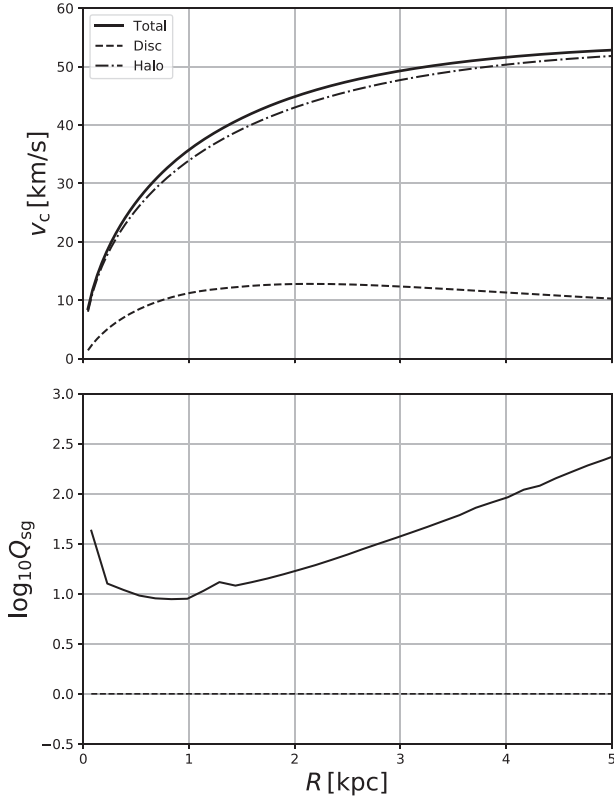
Figure 1. *Top*: The initial circular velocity curve. The solid line is the full dwarf galaxy, while the other lines show the contribution for the other components. *Bottom*: Combined star–gas Toomre parameter using the equation derived by Rafikov (2001).
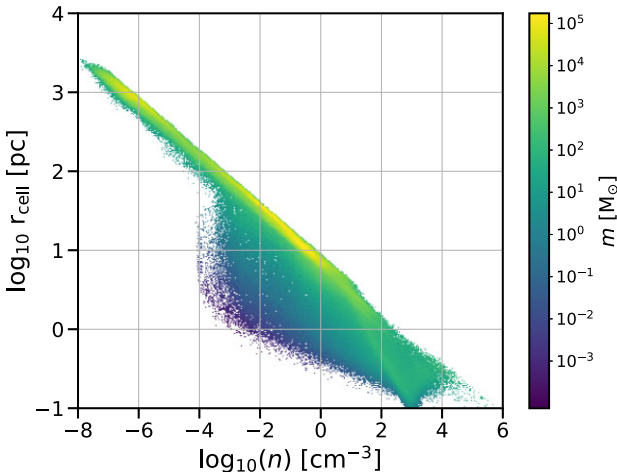

Figure 2. Cell radius as a function of number density. r_{cell} is the radius of a sphere that has the same volume as the cell, taken from the Z.10 G.10 fiducial simulation at 500 Myr. Our refinement scheme devotes most of the computational power to regions of high density where the Jeans length criterion determines the cell mass. In these regions, we reach sub-parsec resolution at densities that are comparable to the sink formation threshold of 10^4 cm^{-3}.

3 RESULTS

In this section, we look at the resulting star formation of the dwarf galaxy models. We first investigate the morphology, general

structure, and evolution of the galaxies. We then look at the effect that varying the parameters has on the underlying chemistry, mass fractions, and phases of the ISM. Finally, we focus on the SFR and how the different metallicities and UV fields affect the KS relationship.

3.1 Morphology

We run the simulations for 1000 Myr, allowing a steady state to develop in all runs, which we find is achieved for the SFR after 300 Myr. In all four models, we have an initial burst of star formation during the first 200 Myr. This arises due to the lack of supportive supernova feedback at the beginning of the simulation and leads to rapid collapse of the gas and sink particle formation. After a few Myr, the sinks evolve to the point where SNe can occur. This releases large amounts of thermal and kinetic energy into the disc in a short period of time. The SNe push the gas out of the central regions, creating high-density gas at the edge of a void within a few tens of Myr. All star formation happens within these dense regions at this time. Over time, the gas falls back into the galaxy centres, until by 500 Myr there is little evidence of the initial burst in the morphology of the gas. We define the steady-state period based solely on the SFR and not the overall morphology of the gas. As the burst is a consequence of our initial conditions, we focus our analysis of star formation on the steady-state part of the evolution.

Visually, the distribution of H_2 in Fig. 3 differs substantially between the different models. As expected, there is more H_2 in the $0.1 Z_\odot$ models than in the $0.01 Z_\odot$ models. In the G.10 models, we see smaller regions of H_2, with it residing mostly in a thin layer in the disc. While in the G.01 simulations there is a greater distribution of H_2, it is more dispersed and broadly follows the HI distribution. Looking through the plane of the galaxies (Fig. 4), we can see that in the G.01 simulations, the H_2 is dispersed over greater scale heights.

Fig. 5 shows the radius (R_{95}) within which 95 per cent of the mass of H_2 (solid lines), sink particle mass (dotted lines), and HI (dashed lines) is contained. After 300 Myr, a steady state forms. In all simulations, the HI radii are relatively stable or smoothly varying, with the radius decreasing in the $0.1 Z_\odot$ models to roughly the same radius as the $0.01 Z_\odot$ models by 600 Myr. For H_2, R_{95} is approximately constant throughout, with only very small-scale variations due to the stochastic nature of the star formation within. In all cases, the H_2 resides at substantially smaller radii than the HI by at least a factor of 2.

The metallicity is a greater determinant of the H_2 and sink particle R_{95} radius than the UV field. In the $0.01 Z_\odot$ models, the H_2 is confined to radii of 1 kpc or less. For the $0.1 Z_\odot$ models, the H_2 lies at radii of 2 kpc or less. In this case, the UV field plays a larger role, with the G.10 model lying slightly below the G.01 model (Table 4).

The most noticeable impact on the morphology is where the active star formation regions lie, as traced by the sink particles. Table 4 compares the R_{95} radius of the gas phases discussed above, with the radius within which 95 per cent of the sink mass is enclosed. In all cases, the R_{95} for the sinks is very similar to that for the H_2 and much smaller than that for HI. In fact, the sink R_{95} value is slightly larger than that of the H_2 due to sinks drifting away from the gas over time. We see from the table that star formation is confined to the central ~2 kpc for the $0.1 Z_\odot$ model and ~1 kpc for the $0.01 Z_\odot$ model.

Fig. 6 shows the average surface density radial profile for the HI, and H_2 over the steady-state period. The HI density profile is largely unaffected by metallicity or UV field, though there is a small increase in the central 1 kpc in the $0.01 Z_\odot$ models. The H_2 profile differs in line with Figs 3 and 5. For the $0.01 Z_\odot$ models, the H_2 drops off
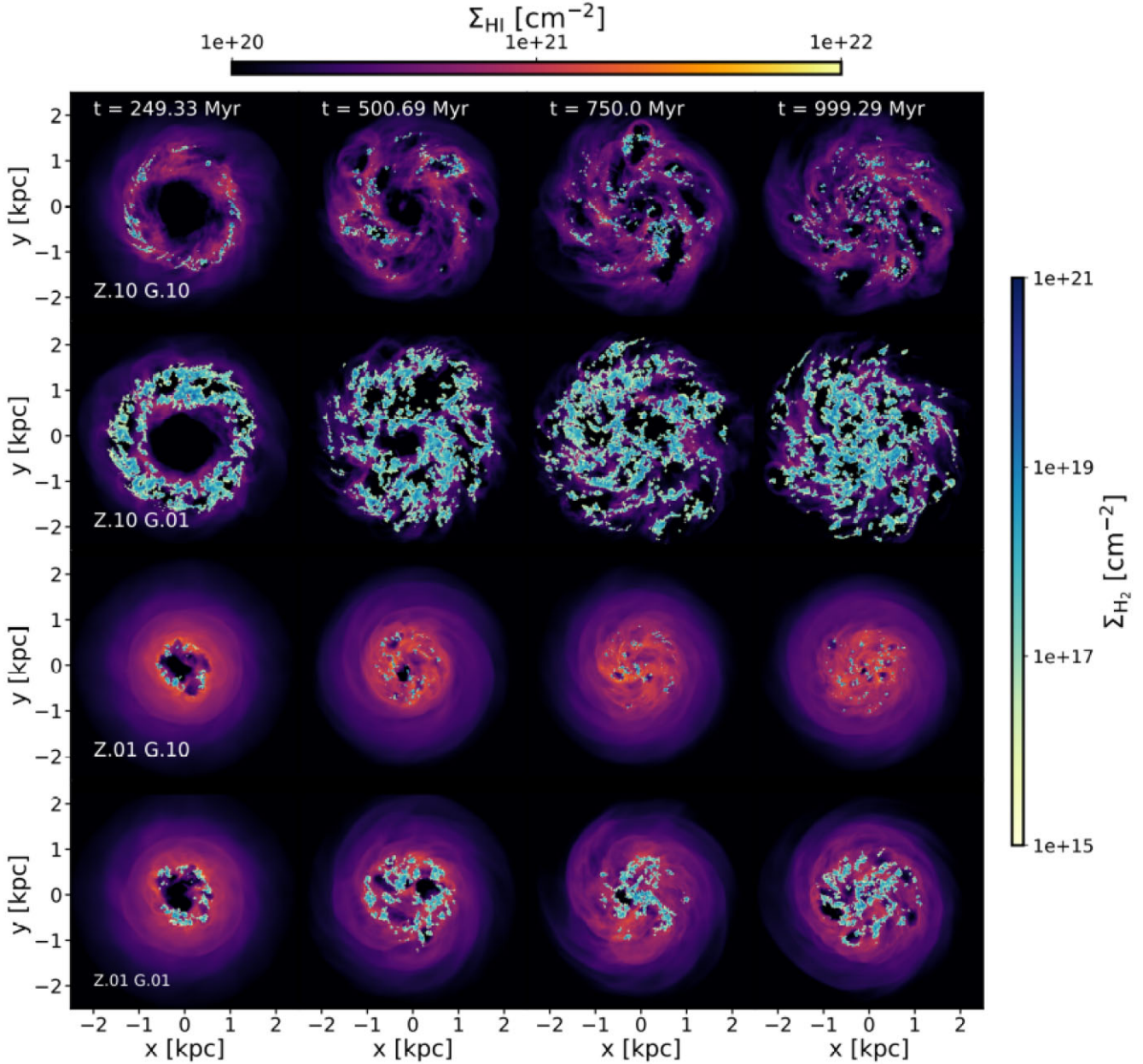
Figure 3. Plots of HI surface density (Σ_{HI}) and H_2 surface density (Σ_{H_2}) for the four simulations. From left to right, we show the disc at times $t = 250$ Myr, 500 Myr, 750 Myr, and 1000 Myr. From top to bottom, the rows correspond to runs Z.10 G.10, Z.10 G.01, Z.01 G.10, and Z.01 G.01. The H_2 surface density distribution varies significantly between the four different runs.

rapidly, but for the $0.1 Z_\odot$ models, we see a more steady decline in surface density out to ~ 2 kpc. Overall, the $0.10 Z_\odot$ models are ~ 0.5 kpc more extended in radius.

3.2 ISM chemistry

In this section, we present the main results of the evolution of the ISM and hydrogen species. We leave a more detailed analysis of the CO chemistry for future work since it is likely that the CO abundances are not fully converged at our current resolution (see e.g. Joshi et al. 2019).

Fig. 7 shows how the H_2 mass fraction evolves with time in the four models in relation to total HI + H_2 gas mass. We note that the mass fraction of H_2 in all models is extremely small and the

ISM is almost entirely dominated by HI. Table 5 shows the average steady-state mass fraction for H_2, the cold ($T < 100$ K) HI + H_2 mass fraction, and the H_2 ($\tau_{dep(H_2)}$) and cold ($\tau_{dep(cold)}$) depletion times, equation (4), in all four models. We also show the standard deviation in the depletion time ($\sigma_{\tau_{dep/ss}}$) as a guide to how much this varies within the discs. There is $\sim 7-8$ times more H_2 in the $0.10 Z_\odot$ models than in the $0.01 Z_\odot$ models. These differences are most likely due to the reduced amount of dust surfaces on which to form H_2 in the lower metallicity case. Similarly, there is more mass in the cold phase in the $0.10 Z_\odot$ models than in the $0.01 Z_\odot$ models. This is a consequence of the longer cooling times in the lower metallicity runs. Gas that has been shock heated or that is cooling from the warm neutral medium to the cold neutral medium following a compression takes much longer to reach a temperature
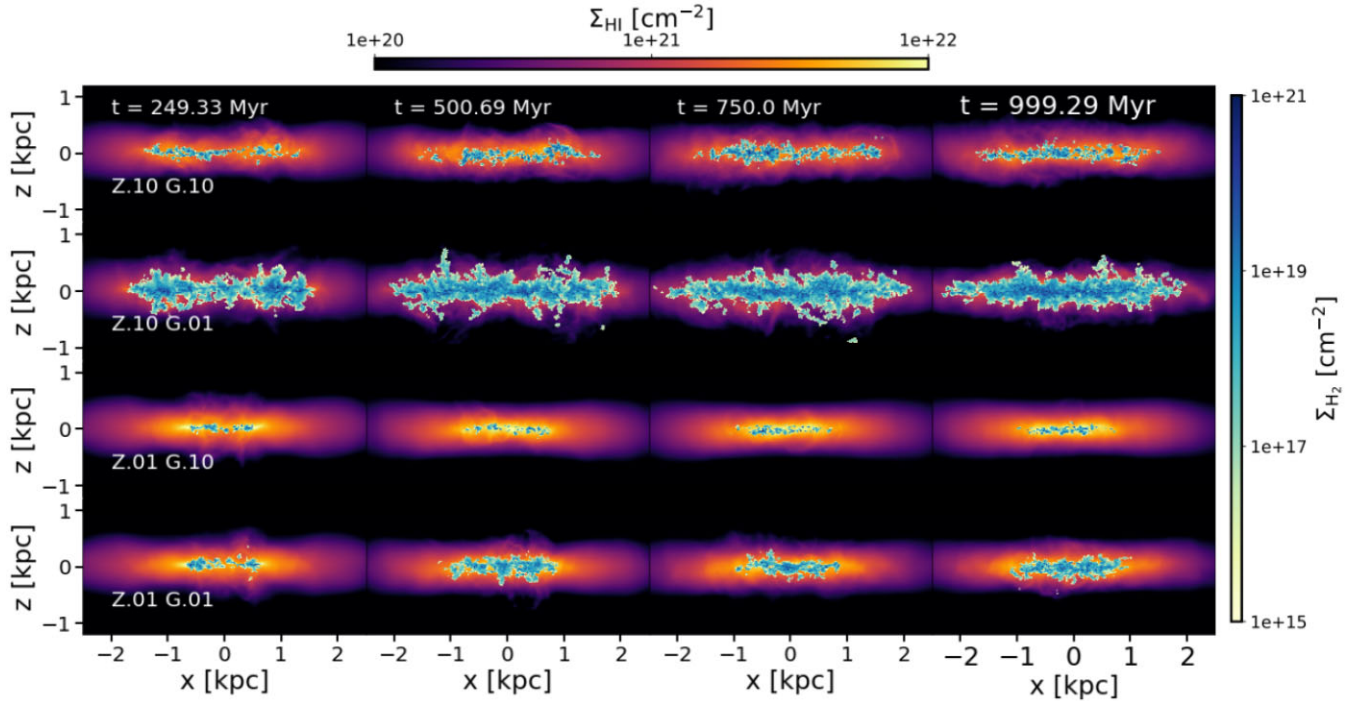
Figure 4. Plots of HI surface density (Σ_{HI}) and H_2 surface density (Σ_{H_2}) for the four simulations shown through the plane. From left to right, we show the disc at times $t = 250$ Myr, 500 Myr, 750 Myr, and 1000 Myr. From top to bottom, the rows correspond to runs Z.10 G.10, Z.10 G.01, Z.01 G.10, and Z.01 G.01. We see that the scale height of the H_2 in the z direction varies substantially from simulation to simulation but displays little variation over time.
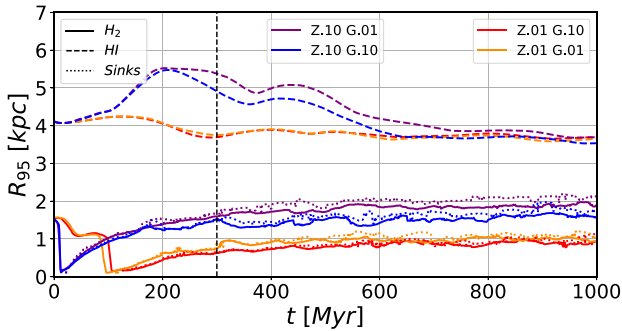

Figure 5. Radius within which 95 per cent of the mass of H_2, HI, and sinks lie over the duration of the simulations. The blue line is the Z.10 G.10 model, the purple the Z.10 G.01 model, the orange the Z.01 G.01 model, and the red the Z.01 G.10 model. The vertical dashed line represents the time at which we consider the steady state to begin. The values of R_{95} for the H_2 and the sink particles are very similar and are stable over time. Both are at least a factor of 2 smaller than the value of R_{95} for the HI.
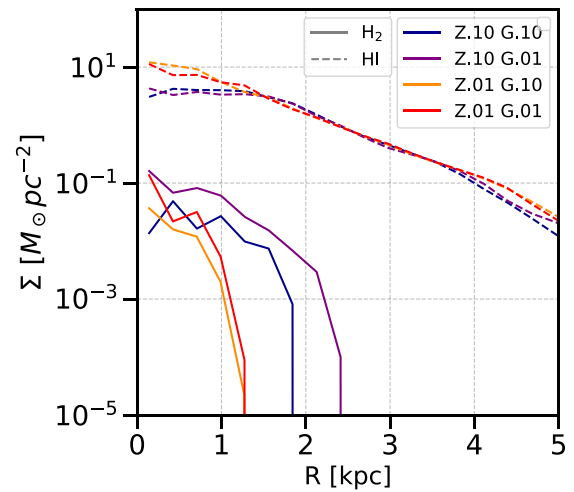

Figure 6. Average surface density radial profiles for the four simulations over the steady-state period. The plot shows Σ_{H_2} and Σ_{HI}. The Σ_{HI} profile is more extended and has greater surface density than the Σ_{H2} profile.

Table 4. Average steady-state radius in kpc within which 95% of the mass lies for HI, H_2, and sink particles for each of the four simulations. Metallicity has a greater impact than G_0 on the values of R_{95} for the H_2 and the sink particles.

	R_{95} HI (kpc)	R_{95} H_2 (kpc)	R_{95} sinks (kpc)
Z.10 G.10	4.03	1.50	1.65
Z.10 G.01	4.30	1.81	2.00
Z.01 G.10	3.76	0.83	0.92
Z.01 G.01	3.74	0.93	1.07

of <100 K in these runs because there is little carbon or oxygen present to provide fine structure cooling. Therefore, even though the equilibrium temperature at each density varies only weakly with metallicity, the end result of reducing the metallicity is a reduction in the cold gas fraction. We also see that when we reduce the strength of the UV field by a factor of 10, we roughly double both the H_2 mass fraction (owing to the lower photodissociation rate) and the cold gas mass fraction (owing to the change in the photoelectric heating rate.

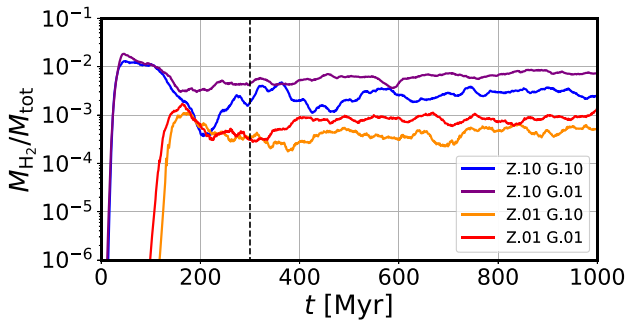$$\tau_{dep(gas)} = \frac{M_{gas}}{SFR}. \tag{4}$$

Figure 7. Mass fraction for H_2 for all four models. There is a higher mass fraction of H_2 in the $0.10\,Z_\odot$ models.
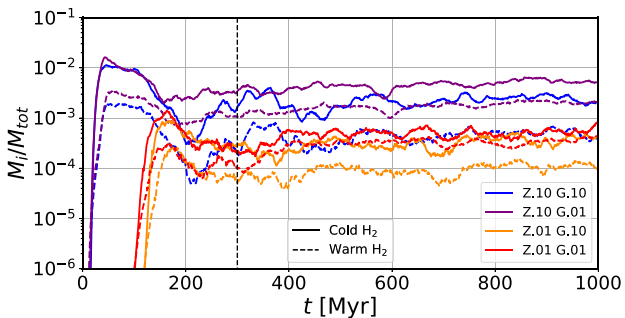

Figure 8. ISM temperature phase plot showing the mass fraction in the cold and warm phase, which is considered to be below 100 K. The warm phase as it is dominated by HI.

We note that as sink particles form in the coldest and densest regions of the ISM, they remove gas from these regions and lock it into collisionless particles. Unfortunately, we have no information on the density, temperature, or chemical composition of the trapped gas. Our sink particles have a formation radius of 1.75 pc and a proportion of the gas in this region may be molecular. Since we do not know the exact fraction that this corresponds to, we ignore any gas inside the sink in our main analysis. Thus, our results are a lower limit on the molecular gas. In Appendix B, we consider how our results would change if the gas mass of young sinks (less than 3 Myr old) that have not had SNe were included in our molecular total, in line with Olsen et al. (2021), a procedure that gives us an upper limit on the molecular gas mass. We do not include this contribution by default as it is unclear precisely how much of the gas locked up in the sinks is actually molecular.

We also examine the temperature phases of the ISM as a function of mass fraction of the total (HI + H_2) gas. Fig. 8 shows two regimes, cold (below 100 K) and warm ($100-10^{4.5}$ K). We do not consider the hot phase in this work as it is not relevant for the results discussed here. Like the H_2 mass fraction in Fig. 7, the cold gas mass fraction shows small variations over the steady-state period. Both plots are

very similar, but the absolute values of the total cold gas fraction are higher than that of the H_2. Although there is a factor of 10 reduction in the metallicity between the Z.10 G.10 and Z.01 G.01 models, there is only a factor of 2–3 reduction in the amount of H_2 and cold gas. However, it should be remembered that the warm gas and HI dominate in all simulations, with both the H_2 and cold gas having negligible mass fractions.

Fig. 9 shows the H_2 mass-weighted phase diagrams (temperature versus number density). The majority of H_2 lies in the cold gas, with a large proportion of the mass below $T = 100$ K. In the low UV field models, we see a more diffuse distribution, with a significant fraction of the molecular gas in the warm phase, $T = 100-10^{4.5}$ K, owing to the less effective photodissociation of H_2 in these runs. The H_2 distribution does not solely reside in the conditions typical of star-forming regions ($T < 100$ K and $n > 100\,\text{cm}^{-3}$). This is especially true in the low UV field models, where non-star-forming regions can contain a substantial fraction of the total amount of H_2 present in the disc.

Fig. 10 shows the H_2 and cold gas depletion times for all four models. The H_2 depletion times for the $0.10\,Z_\odot$ models are over an order of magnitude faster than the values commonly observed in local spiral galaxies ($\tau_{\text{dep}} \sim 2.0 \times 10^9$ yr) (Bigiel et al. 2008; Leroy et al. 2008), and those for the $0.01\,Z_\odot$ runs are smaller still. The cold gas depletion times are of less than an order of magnitude faster than that observed in solar metallicity spirals. However, as we will see later, this is not because star formation is more efficient in these systems. Rather, it is because the stars that are forming in these low metallicity systems are forming in cold HI-dominated gas, and so the H_2 depletion time gives a misleading view of how rapidly the gas is actually being consumed. Unlike in Tress et al. (2020), who use the same sink particle and feedback mechanisms, we do not see a decrease in τ_{dep} over time. In their simulation, this occurred because over the course of the simulation, the ongoing star formation appreciably depleted the amount of gas available for forming further stars. This does not happen in our simulations owing to the much smaller SFRs involved, as we discuss further in the next section.

3.3 Star formation

In this section, we present the results of our star formation model and how it is affected by the different conditions. For our SFR, we use the stellar component of the sink particle mass ($\epsilon_{\text{SF}} \times$ total sink mass) and convert it into a rate by taking the stellar mass accreted ($M_{\odot,\text{acc}}$) on to the sink particle at each snapshot plus any new sinks created ($M_{\odot,\text{new}}$) and dividing by the time difference between each current snapshot (t_2) and previous snapshot (t_1):

$$\text{SFR} = \frac{\left(M_{\odot,\text{acc}} + M_{\odot,\text{new}}\right)}{t_2 - t_1}. \quad (5)$$

In Fig. 11, we show the steady-state period for the SFR as a function of time. The shaded regions show the 1σ deviation. The bursty nature of SF is clear in this plot.

Table 6 shows the average steady-state star formation rate (SFR_{ss}) and the standard deviation (σ_{ss}) for each model, along with the HI

Table 5. Mass fractions and depletion times for H_2 and cold HI + H_2 gas. There is a smaller H_2 mass fraction and depletion time in the $0.01\,Z_0$ models. The cold gas depletion times are greater than the H_2 due to this being HI dominated.

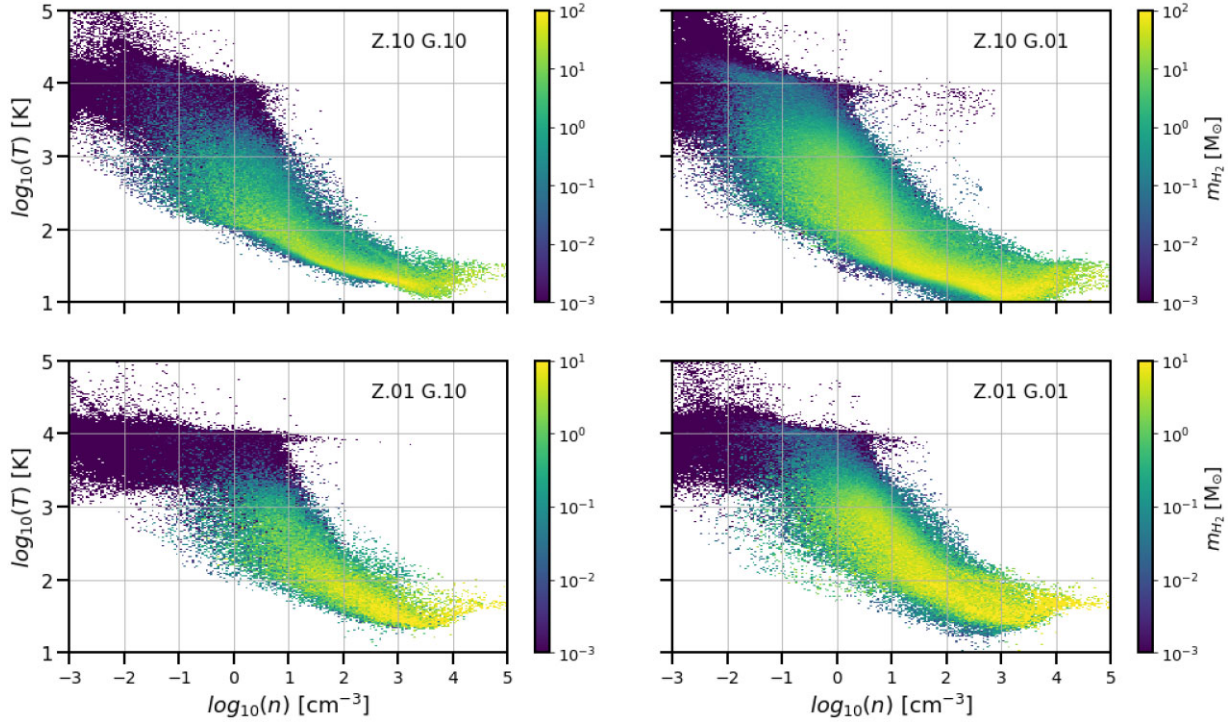|	M_{H_2}/M_{HI+H_2}	$M_{\text{cold}}/M_{HI+H_2}$	$\tau_{H_2\text{dep/ss}}$ (yr)	$\sigma_{\tau_{H_2\text{dep/ss}}}$	$\tau_{\text{colddep/ss}}$ (yr)	$\sigma_{\tau_{\text{colddep/ss}}}$
Z.10 G.10	0.27%	1.66%	9.16×10^7	2.63×10^7	5.66×10^8	1.65×10^8
Z.10 G.01	0.63%	4.26%	1.18×10^8	2.56×10^7	8.04×10^8	1.77×10^8
Z.01 G.10	0.04%	0.29%	5.25×10^7	3.72×10^7	3.75×10^8	2.68×10^8
Z.01 G.01	0.08%	0.58%	3.54×10^7	1.73×10^7	2.57×10^8	1.61×10^8

Figure 9. H_2 mass-weighted phase diagrams at $t = 500$ Myr. The majority of the H_2 mass lies in the cold ($T < 100$ K) gas, but there is also a significant proportion of it in the warm diffuse phase in the G.01 models that arises due to the lower photodissociation rates in the very low G_0 simulations.
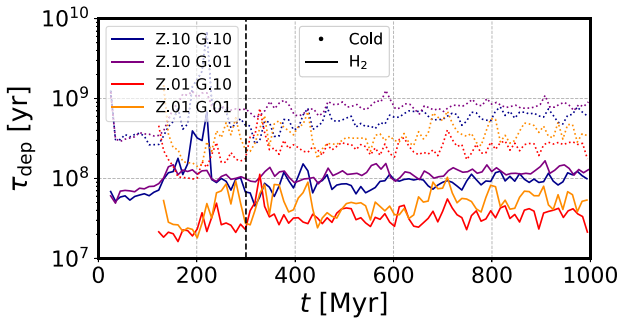

Figure 10. Depletion time ($\tau_{\rm dep}$) for H_2 and cold gas as a function of time. $\tau_{\rm dep}$ is shorter and more variable when we lower the metallicity of the models, but there is little change when the UV field strength is lowered.
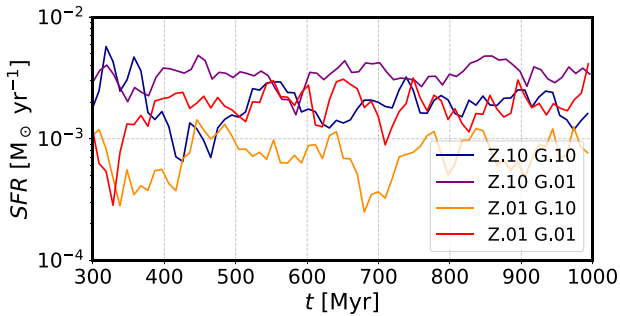
Figure 11. The star formation rate for the four models over the steady state period. The SFR of the Z.10 G.10 and Z.01 G.01 models is very similar.

$+ H_2$ surface density ($\Sigma_{\rm HI+H_2}$) and H_2 mass fraction for comparison. There is little variation in the average $SFR_{\rm ss}$ across the models. The key result is the similarity between the Z.10 G.10 and Z.01 G.01 models, where a factor of 10 reduction to both parameters has a negligible effect on the SFR, with both lying well within $\sigma_{\rm ss}$ of each other. Comparing the $SFR_{\rm ss}$ with the $\Sigma_{\rm HI+H_2}$ and $M_{H_2}/_{\rm total}$ values in Table 6, there is little connection to the total gas surface density, but there is a simple correlation to the H_2 mass fraction as when the $SFR_{\rm ss}$ is increased, so is the mass fraction.

The $SFR_{\rm ss}$ for all four models are highly variable, or bursty over the steady-state period. This is particularly true of the Z.01 G.10 model, where there are periods where the SFR falls well below 10^{-3} $M_\odot$ yr^{-1}.

Fig. 12 shows the total mass of stars formed in each simulation over the steady-state period. There is again a clear similarity between the Z.10 G.10 and Z.01 G.01 simulations, showing that the factor of 10 reduction in metallicity and UV field has had little effect on the total mass of stars formed. There is, however, a larger variation in the mass of stars formed when we vary the parameters separately, showing that the SFR is sensitive to a change in both the UV field and the metallicity. In the two models where these quantities are varied independently, we see a factor of $\sim$5 difference in the SFR at 1 Gyr.

3.4 Kennicutt–Schmidt relationship

In this section, we examine the molecular gas KS relationship for each model. Fig. 13 shows the KS relationship when averaging over a bin area of $(500{\rm pc})^2$.[1] The bins are evenly spaced boxes over the

[1]In Appendix A, we investigate the effects a larger bin of $(1{\rm kpc})^2$ would have upon our results as an analogy to using different telescope beam widths.

Table 6. Average steady-state star formation rates, SFR_{SS}, the size of the 1σ standard deviation as a percentage of SFR_{SS}, HI + H_2 surface density (Σ_{HI+H_2}), H_2 surface density (Σ_{H_2}), and H_2 mass fraction.

	SFR_{SS} ($M_\odot yr^{-1}$)	σ_{ss}	Σ_{HI+H_2} ($M_\odot pc^{-2}$)	Σ_{H_2} ($M_\odot pc^{-2}$)	M_{H_2}/M_{HI+H_2}
Z.10 G.10	2.01×10^{-3}	47.4%	2.50	8.27×10^{-3}	2.7×10^{-3}
Z.10 G.01	3.41×10^{-3}	26.7%	2.40	10.67×10^{-3}	6.3×10^{-3}
Z.01 G.10	7.65×10^{-4}	50.2%	3.25	3.10×10^{-3}	0.4×10^{-3}
Z.01 G.01	1.90×10^{-3}	42.8%	3.11	5.78×10^{-3}	0.8×10^{-3}
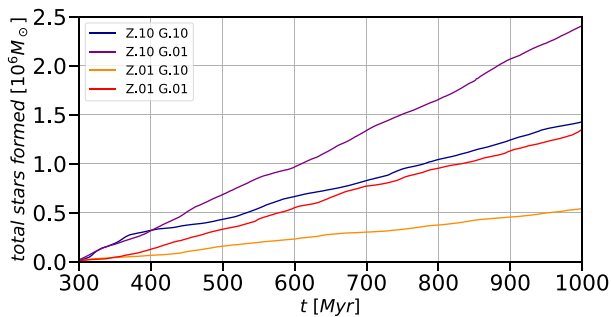
Figure 12. The cumulative mass of stars formed for the four models over the steady-state period, which we take to start at $t = 300$ Myr. The similarity between the Z.10 G.10 and Z.01 G.01 models is clear.

disc, within which the average gas column density and SFR are calculated. We stack data over the whole steady-state period of the simulations, taking data every Myr, to ensure a complete sampling of the data; see Appendix A for an analysis of the time evolution. The colours represent the different models in the same format as all other figures. The grey dashed lines represent a linear relation of $N = 1$, as found by Bigiel et al. (2008) for a combination of spirals and late-type/dwarf galaxies when considering H_2 surface density (Σ_{H_2}) with an aperture size of 400 pc for a variety of different depletion times. For reference, the depletion time suggested by Bigiel et al. (2008) is approximately 2 Gyr. Our cold gas depletion time is almost an order of a magnitude faster than this, suggesting that the efficiency of forming stars in cold gas is similar in low-metallicity dwarf galaxies and higher-metallicity spirals, and that the low depletion times we see for the H_2 in the dwarfs are because the stars are forming in regions dominated by HI rather than because the H_2 is able to form stars more efficiently in these systems.

Table 7 shows the best-fitting power-law indices and the 1σ standard deviation. The power laws are fitted using the SCIPY linear regression module and the standard deviation is taken over the whole data set using NUMPY. For our fiducial case (run Z.10 G.10), the power-law slope for molecular hydrogen is almost linear with $N_{H_2} = 1.09$. However, as the metallicity and UV field strength are changed, there are small departures from this. Lowering the field strength steepens the slope slightly to $N_{H_2} = 1.18$. When the metallicity is reduced, variations become more pronounced. In run Z.01 G.10, the slope becomes mildly *sub-linear*, whereas run Z.01 G.01 has the steepest slope.

Table 7 also shows the power-law slopes that would be found if instead of the H_2 column density, we considered cold gas ($T < 100$ K). The values of N_{COLD} are always super-linear and are consistently higher than N_{H_2}. Thus, there is proportionally more cold gas at higher column densities per unit star formation than there is molecular hydrogen.

We do not fit a slope to Σ_{total} due to the limited column density range over which most of the data lie, meaning that any fit is likely

to be determined purely by the large scatter in our data and will therefore be inaccurate.

4 DISCUSSION

We have run four hydrodynamical models of metal-poor dwarf galaxies varying both the metallicity and the UV fields. They were run for 1 Gyr and analysed over a steady-state period that began after 300 Myr. We present here a discussion on the key points in this paper.

4.1 Morphology

Comparing the morphology of our simulations to those of Hu et al. (2016) and Hu et al. (2017), we note little difference in the models that have similar conditions. Across our four models, the surface density radial profiles and scale heights are similar to their works. In agreement with their work, we find that the SFR and the general properties of the gas distribution reach a steady state after around 300 Myr.

All four models are dominated by HI, which shows high-density structures and SN-driven voids (see Fig. 3). Before the steady-state period begins, we can see the H_2 traces the dense HI regions formed by the initial starburst. Fig. 14 shows that H_2 does not always trace the densest regions of HI. For example, there is a dense H_2 cloud that appears to be in a void, though the mean column density in this void is around 10^{19} cm^{-2}. This occurs due to the HI being more easily disrupted by SNe.

Star-forming regions (represented by sink particles in our simulations) can drift apart from both the HI and H_2 gas as shown by their greater radial extent in Table 4. Some of this is due to SNe occurring around the sink particle driving away the HI and creating the voids. Our sink particles are purely gravitational objects but the gas experiences additional hydrodynamic forces, which can also cause the two distributions to decouple. Fig. 14 shows the location of sink particles in red, compared to the H_2 in blue. For the most part, the sinks lie at the centre of H_2 clouds, but there are instances where the sink is at the edge of a molecular region, or entirely separate from them. This is most likely due to the decoupling effect. However, it is theoretically possible for a sink to form in purely atomic gas as our sink formation criteria depend on the boundedness of the gas and not on its molecular content. We will investigate the local environment of star formation within our dwarf galaxies in more detail in future work.

4.2 ISM chemistry

The key points we take away from our treatment of the ISM and varying the metallicity and UV field strength are that a factor of 10 reduction in both variables has a large impact on the H_2 formed in the galaxy. As we decrease Z or increase the field strength, the molecular gas becomes more closely confined to the galaxy centre (as seen by the shrinking of R_{95}).
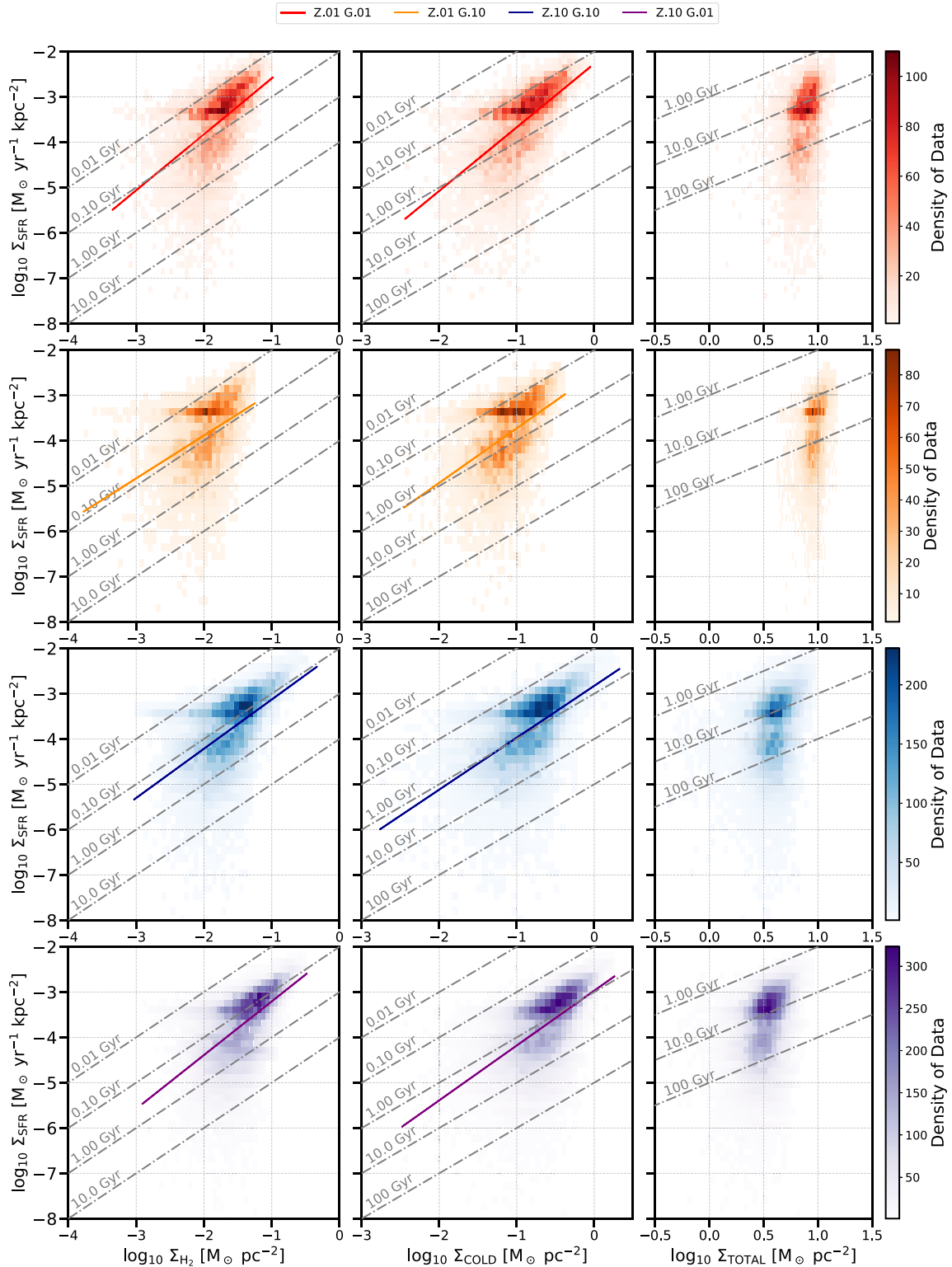
Figure 13. The Kennicutt–Schmidt relationship for the steady-state time period for each model, averaging over a bin area of $(500\text{pc})^2$. From left to right, we show N_{H_2}, N_{COLD} (where we define the cold phase to be all gas with $T < 100$ K), and N_{total}, where the total surface density includes all of the H and H_2, regardless of density, but does not include ionized gas. It is plotted as a heat map with the solid lines showing the best-fitting power law for each simulation, and the grey dashed line represents the $N = 1$ slope for different depletion times. Results for different simulations are colour-coded as indicated in the key. We see that N_{H_2} and N_{COLD} both show linear to super-linear behaviour.

Table 7. Power-law slopes (N) for the Kennicutt–Schmidt law for the four models based on Σ_{H_2} and Σ_{COLD} with the standard errors from linear regression statistics. The molecular and cold KS slope is linear to super-linear, steepening as the UV field strength is reduced.

	N_{H_2} (500 pc)	N_{COLD}
Z.10 G.10	1.09 ± 0.014	1.15 ± 0.014
Z.10 G.01	1.18 ± 0.012	1.21 ± 0.012
Z.01 G.10	0.95 ± 0.027	1.20 ± 0.028
Z.01 G.01	1.24 ± 0.022	1.40 ± 0.021

Table 8. Fraction of the total amount of H_2 in the cold phase ($T < 100$ K) and in the warm phase ($100 < T < 10^{4.5}$ K). The amount of H_2 in gas hotter than $10^{4.5}$ K is negligible. We see that a significant fraction of the H_2 content of each galaxies lies in the warm phase, particularly in run Z.01 G.01. Nevertheless, the majority of the H_2 is found in the cold phase in each case.

	Cold H_2	Warm H_2
Z.10 G.10	83%	17%
Z.10 G.01	73%	27%
Z.01 G.10	77%	22%
Z.01 G.01	60%	39%

In line with previous work, we find that the ISM in our simulated galaxies is dominated by HI, the majority of which is in the warm phase. The cold gas fraction ranges between 0.3 per cent and ~4 per cent, and the H_2 fraction is around 6–7 times smaller still. As expected, both the cold gas and the molecular gas fractions are highest in the Z.10 G.01 model, as it combines the highest metallicity and dust-to-gas ratio of our models with the lowest photodissociation rate.

Fig. 8 shows the phase-space distribution in terms of the density and temperature of the molecular gas. While the bulk of the H_2 lies at temperatures below 100 K and would therefore be considered cold gas in our analysis, there is still a noticeable component at higher temperatures. This is particularly true in the simulations with lower UV field strengths, where there is a larger warm diffuse component to the H_2. For example, in the Z.01 G.01 model, 39 per cent of the H_2 lies in the warm phase and 61 per cent in the cold phase (Table 8).

In contrast to many previous studies, our sink particle-based prescription for star formation does not prescribe a depletion time in cold and/or molecular gas, allowing us to explore how this varies in our simulated galaxies as a function of metallicity and UV field strength. Looking at Table 5 and Fig. 10, we see that the molecular gas depletion time decreases significantly with decreasing metallicity. However, this behaviour merely reflects the fact that the dense clouds in which the stars form are dominated by atomic gas. Decreasing the

metallicity decreases the molecular content of the clouds (because of the reduction in the dust content of the gas and hence the H_2 formation rate) but does not strongly affect the rate at which these clouds form stars, as we discuss in more detail below. This can be seen quite clearly if we look at the cold gas depletion times, which range from $\sim 3 \times 10^8$ yr to 10^9 yr. These values are still somewhat smaller than the value of 2×10^9 yr typical of molecular gas in late-type spiral galaxies (Bigiel et al. 2008) but are an order of magnitude larger than the H_2 depletion time.

It is also interesting to compare the total gas depletion times from all models (Fig. 15) with the total gas depletion times measured in the HI-dominated dwarf galaxies in the FIGGS survey (Roychowdhury et al. 2015). In our simulations, we typically find values between 10^{10} yr and a few times 10^{10} yr, in good agreement with the FIGGS results for galaxies with a similar mean gas surface density (see e.g. figs 4 and 5 in Roychowdhury et al. 2015).

4.3 Star formation

Despite the large reduction in the H_2 mass, *the SFR is essentially unchanged* between the Z.10 G.10 and Z.01 G.01 models. This shows that the relationship between H_2 and star formation breaks down at low metallicity and low UV field strength. This is in line with the work of Glover & Clark (2012b) and Hu et al. (2016). We also
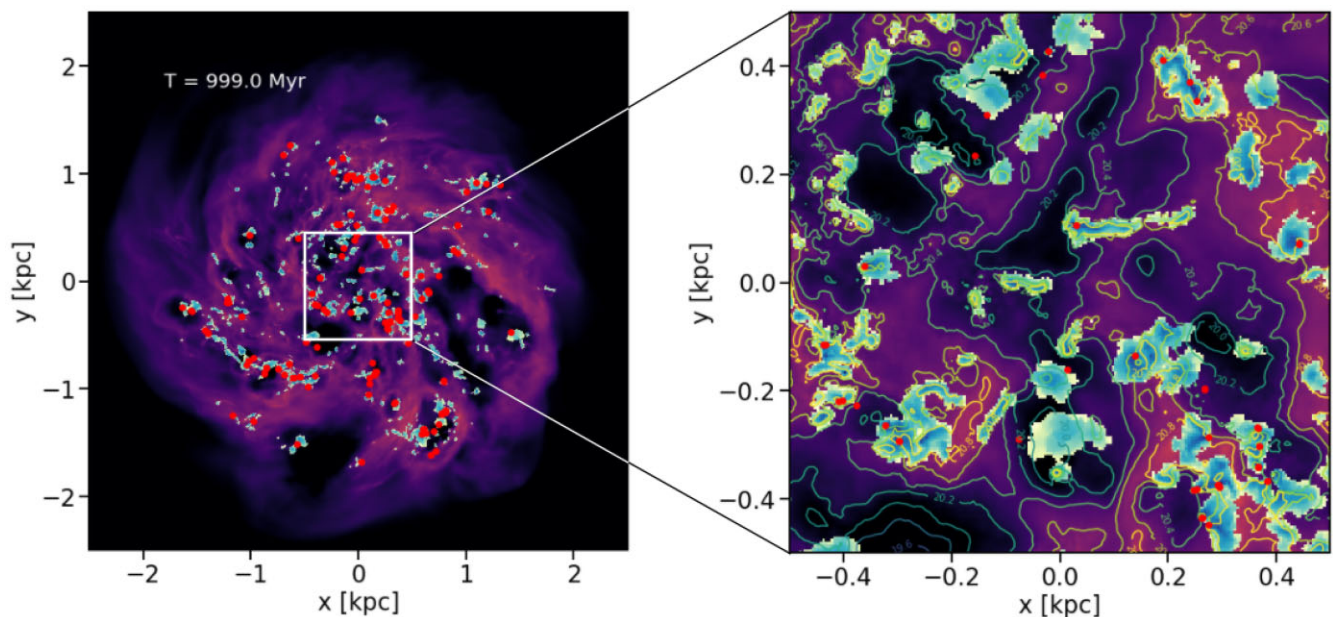

Figure 14. A closeup of the central 0.5 kpc region of simulation Z.10 G.10 with sink particles shown as red dots. It shows that some sink particles are situated in the voids, while some remain in the dense gas.
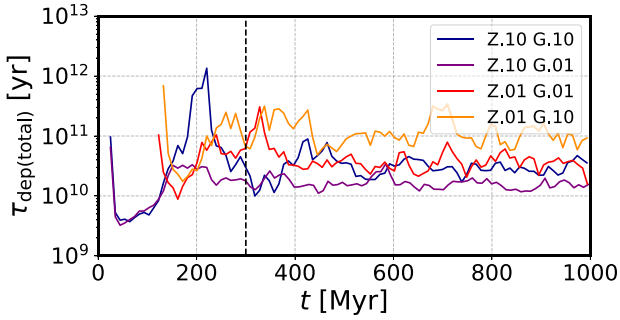
Figure 15. Depletion time for the total gas.

note an agreement with Krumholz (2012), who predicted that at low metallicities, star formation should become increasingly associated with cold atomic gas. A greater effect upon the star formation is seen when the metallicity and the UV field are varied independently of each other. Reducing the UV field, for a constant metallicity, raises the SFR, as the reduced photoelectric heating rate makes it easier to form cold, dense clouds in the ISM. On the other hand, reducing the metallicity, for a constant UV field, lowers the SFR, since the increase in the cooling time makes it harder to form cold clouds. When both variables are varied, their impacts cancel out to a large extent.

An obvious question then arises: what is the most realistic combination of variables in the extremely metal-poor case? The UV field should in reality be generated by the stars. Since the SFR surface density we find in our simulated galaxies is roughly an order of magnitude smaller than that found in the discs of typical metal-rich spirals (Bigiel et al. 2008), we would therefore expect the UV field strength to be approximately an order of magnitude smaller as well. Therefore, we expect that the true UV field should on average look more like the value used in our G.10 runs than in our G.01 runs.

In our study, we keep the cosmic ray ionization rate selected for each simulation fixed as a function of time and position and do not include cosmic ray injection from SNe. A recent study by Dashyan & Dubois (2020) shows how SNe-driven cosmic rays can affect the SFR in a large magnetohydrodynamic (MHD) dwarf galaxy simulation where they note a factor of $\sim$2 reduction in the SFR when this is included. This likely means that our SFR_{ss} are an overestimation but are still consistent with other comparable simulations. Jeffreson

et al. (2021) show that by adding in HII momentum feedback in a Milky Way-like galaxy at varying resolutions, there is no effect on the SFR. This allows us to be confident that our SFRs and models would be unaffected by additional feedback mechanisms other than SNe-driven cosmic rays.

Table 9 shows a comparison between our simulated SFR_{ss} and surveys of Local Group dwarf galaxies. It is clear that there is great variability in $Z_{\odot}$ and SFR, making a direct comparison difficult. For the small magellanic cloud (SMC), with a mass of 4.20×10^8 $M_{\odot}$ and $Z = 0.1 \, Z_{\odot}$, the literature shows the SMC to have two star formation epochs: one 6 Gyr ago, during which the average SFR was approximately 0.3 $M_{\odot} yr^{-1}$ and a more recent one at 0.7 Gyr ago with a similar value for the SFR (Rezaeikh et al. 2014). During these bursts of star formation, the SMC has an SFR two orders of magnitude higher than we see in our simulations. Rezaeikh et al. and others note that this high SFR is likely to have arisen because of interactions with the large magellanic cloud (LMC) and the Milkyway (MW) and note an overall SFR of $\sim 0.1 \, M_{\odot} yr^{-1}$.

We can also compare the SFRs in our simulated galaxies to those measured in NGC 147 and NGC 185, two satellite galaxies of Andromeda with similar masses to the SMC, but lower metallicities (Hamedani Golshan et al. 2017). One thing of note in their star formation history is an initial burst in SF early in their life, which then becomes steady later on, similar to our simulations. Their SFRs are $\sim 2 \times 10^{-3} \, M_{\odot} yr^{-1}$ for NGC 147 and $\sim 5 \times 10^{-3} \, M_{\odot} yr^{-1}$ for NGC 185. These values are comparable to the SFR_{ss} rates we see in our models.

It is clear that there is little-to-no direct connection between metallicity, SFR, or mass on this small sample. No numerical scaling between the mass and the SFR is noted, though it could be roughly assumed that more mass equates more star formation. NGC 147, however, does not follow this trend as it is twice as massive as our models but shows the same SFR. We also see that the specific SFR across our simulations and observations are comparatively similar.

4.4 KS relationship

The customized version of AREPO used here, with time-dependent chemistry and the identification of bound collapsing regions via sink particles, allows us to produce a KS relationship that arises solely due to the star formation process with few assumptions.

Table 9. Comparing the steady-state SFRs, metallicities, masses, and specific SFR of our models against some observed values. We use the value from our fiducial run for the SFR scaling (2×10^{-3}). The values for the Milky Way come from Kennicutt & Evans (2012) for the gas mass and star formation rate and Ness & Freeman (2016) for an estimate on the global metallicity of the Milky Way. The LMC values are from Harris & Zaritsky (2009), the SMC ones from Harris & Zaritsky (2004), the SFRs for NGC 147 and NGC 185 come from Hamedani Golshan et al. (2017), and estimates of their metallicities are taken from Crnojević et al. (2014). The specific SFRs are calculated by dividing the SFR by the total mass of the galaxies as presented in column one of this table. There are all very similar with little variation across the models and different galaxies.

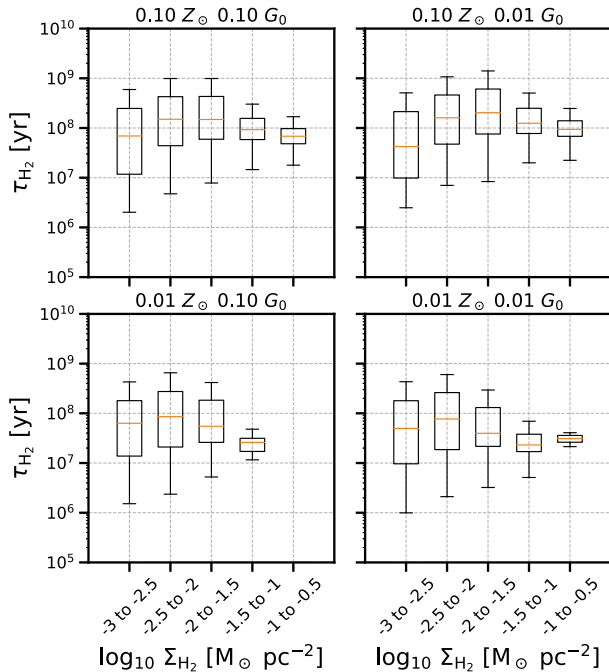|	Mass ($M_{\odot}$)	SFR_{ss} ($M_{\odot} yr^{-1}$)	$Z_{\odot}$	Specific SFR_{ss} (yr^{-1})
Z.10 G.10	8.0×10^7	2.01×10^{-3}	0.10	2.5×10^{-11}
Z.10 G.01	8.0×10^7	3.41×10^{-3}	0.01	4.3×10^{-11}
Z.01 G.10	8.0×10^7	7.65×10^{-3}	0.10	9.7×10^{-11}
Z.01 G.01	8.0×10^7	1.90×10^{-3}	0.01	2.4×10^{-11}
Milky Way	9.5×10^{10}	8.25	1	8.7×10^{-12}
LMC	2.7×10^9	0.2	0.4	7.4×10^{-11}
SMC	4.2×10^8	0.1	0.1	2.4×10^{-10}
NCG147	1.6×10^8	2×10^{-3}	0.1	1.3×10^{-11}
NGC 185	2.4×10^8	5×10^{-3}	0.08	2.1×10^{-11}

Figure 16. Local 500-pc scale H_2 depletion times binned in relation to H_2 column density. In all models, we see a short depletion time in the most diffuse and densest H_2 with the longest times at intermediate column densities.

Figure 17. As Fig. 16, but for the depletion time and surface density of the cold gas. In all models, we see a similar trend to the H_2 gas with shorter depletion time in the most diffuse and densest cold gas. The values are fairly consistent across column densities in the $0.10\,Z_\odot$ models but show more variability in the $0.01\,Z_\odot$ models.

Our results are in line with others in the literature (Bigiel et al. 2008; Kennicutt & Evans 2012; de los Reyes & Kennicutt 2019) in showing a linear to super-linear KS relationship with respect to both molecular hydrogen and cold gas. The slope becomes steeper for lower metallicity or lower UV field strength. While we use a linear regression analysis to match observational data, it should be noted that Shetty et al. (2014) applied a Bayesian analysis to a sample of nearby disc galaxies from the STING survey (Rahman et al. 2012) and found a sub-linear slope of $N = 0.76$ for Σ_{H_2}.

A one-to-one correlation between molecular gas surface density and SFR has been interpreted as showing that H_2 is a necessary precursor of star formation (Bigiel et al. 2008; Pessa et al. 2021). However, this is clearly not the case in our simulations. Although we recover a close to linear relationship between SFR surface density and H_2 surface density in each of our simulations, the normalization of this relationship – the H_2 depletion time – varies substantially as we change the metallicity. This is consistent with the behaviour that we would expect if the true correlation is between cold gas surface density and SFR surface density. In this picture, the correlation with H_2 arises because the surface density of H_2 separately correlates with the cold gas surface density (i.e. $\Sigma_{H_2} \propto \Sigma_{COLD}$), with a coefficient of proportionality – the mean H_2 mass fraction in the cold clouds – that depends on the metallicity and UV field strength.

It is also interesting to explore where deviations from a linear relationship between star formation and cold gas or H_2 arise. To investigate this, we show in Figs 16 and 17 box plots of the local depletion times in 500-pc bins over the steady-state period used to calculate the KS relationships for different column density regimes. In both cases, the depletion times are shorter at lower column densities where it is harder for both H_2 and cold gas to form. Thus, the column density is lower for a given SFR, and the slope becomes
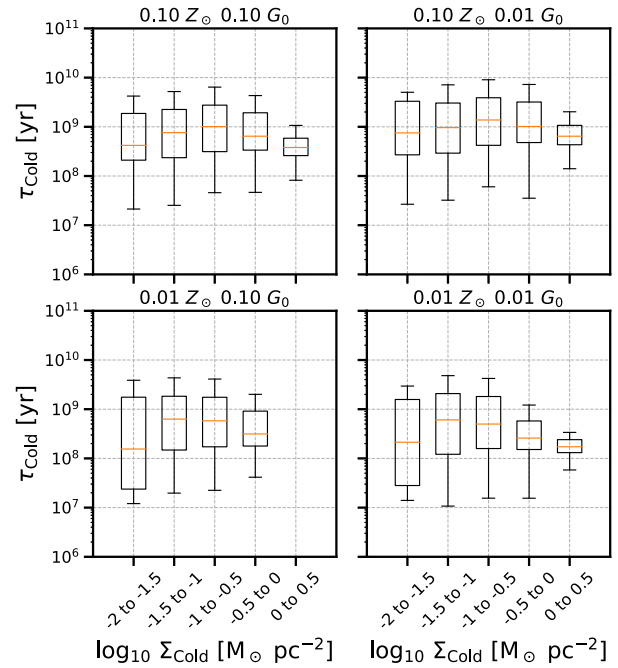
shallower. This appears to be the origin of the sub-linear relation found in run Z.01 G.10, where the ambient UV field is particularly effective at dissociating H_2 and heating the gas.

At high column densities, there is also a reduction in the depletion time, which is likely due to gas being more rapidly consumed by more efficient star formation due to the reduced free-fall time at higher densities. This has the effect of steepening the slope and is more pronounced at lower metallicities where the H_2 and cold gas reservoirs are smaller.

Observationally, it is hard to measure the Σ_{H_2}–Σ_{SFR} KS relationship in dwarf galaxies as H_2 is very difficult to directly detect and other species such as CO are extremely faint. However, the Σ_{HI}–Σ_{SFR} KS relationship has been studied by Roychowdhury et al. (2015) and Filho et al. (2016) and found to be super-linear. Roychowdhury et al. (2015) find a power-law slope of 1.5 looking over different spatial scales for both spiral and dwarf galaxies, which is similar to other works (e.g. Kennicutt & Evans 2012). In addition, Filho et al. (2016) note that XMPs generally follow the literature but there is a fraction that fall off the slope that the authors suggest could be due to CO-dark H_2. de los Reyes & Kennicutt (2019) use various different fits to look at the Σ_{HI}-Σ_{SFR} KS relationship. Each method gives a different slope, but they find that their preferred fitting method gives a value of 1.26 ± 0.08 for a combination of spirals and dwarf galaxies. Comparing this to our results for H_2, they are shallower but lie within 1 standard deviation of the de los Reyes & Kennicutt (2019) result.

4.5 Caveats

The ISM is a complex system that has many active processes occurring within it. Any simulation of this system is inevitably a simplification and ours are no exception. In particular, in our

simulations, we do not currently include MHD, photoionization, or the effects of stellar winds (although the effects of the latter are likely small at these metallicities).

As stated in Section 2.3, we do not form individual stars. Even though simulating a dwarf galaxy allows us to achieve extremely high resolution, we are still limited as to how fine we can go. As a result, we cannot state how the ISM is behaving within the regions represented by the sink particles. In the bulk of this work, we have excluded the sink particles when studying the gas properties, but in Appendix B, we show how the H_2 depletion time and molecular KS relationship change if we assume that all of the non-star-forming gas in the sinks is molecular.

Another simplification made here is our assumption that the UV field is constant throughout the galaxy. This is unrealistic: in reality, it will be stronger closer to regions of active star formation and weaker away from these regions. Similarly, we neglect variations in the metallicity and dust-to-gas ratio within the disc, which is a reasonable description of some dwarf galaxies but not all (see e.g. the discussion in section 5.1 of James et al. 2020).

Finally, we note that as we do not include photoionization in our simulations, we likely overproduce diffuse atomic gas and underproduce diffuse ionized gas, particularly at large scale heights above the disc. However, we know from observations that there is far more atomic gas than ionized gas in most dwarf galaxies, and so we do not expect this limitation to significantly impact our results.

5 CONCLUSIONS

We have modelled four isolated dwarf galaxies for 1 Gyr using the AREPO code. In each simulation, we varied the metallicity and/or the UV field strength. Our models include gas self-gravity, a time-dependent, non-equilibrium chemical network, local shielding, accreting sink particles to model star formation, and SNe tied to the sinks. Our resolution reaches down to sub-parsec scales and resolves the Jeans mass throughout the simulation with a minimum of eight resolution elements. The main results can be summarized as follows:

(i) The discs of our four simulated galaxies are dominated by warm atomic hydrogen. The cold gas mass fraction ranges from <1 per cent to a few per cent, while the H_2 mass fraction is less than 1 per cent in every case. Reducing the UV field strength leads to the formation of more H_2 and more cold gas; conversely, reducing the metallicity decreases the amount of both.

(ii) H_2 is found in the warm phase in all models, particularly the ones with the lower UV field strength. This supports the idea that there is a disconnect between SF and H_2 in extreme conditions.

(iii) The morphology of the H_2 distribution is also sensitive to the UV field strength and metallicity, with the distribution becoming significantly more compact for lower metallicity and/or higher UV field strength.

(iv) The total gas depletion times for all of our models match those seen in observations of HI-dominated dwarf galaxies, showing that our models compare well with real data.

(v) The H_2 depletion time varies with the metallicity. However, this merely reflects a change in the average H_2 mass fraction in the star-forming clouds rather than any substantial change in their ability to form stars. In support of this, we note that the cold gas depletion time shows much less variation than that for the H_2.

(vi) A factor of 10 reduction in both metallicity and UV field strength has no significant effect on the SFR. However, the SFR does differ if these quantities are varied independently of one another.

(vii) The Σ_{SFR}-Σ_{H_2} KS relationship is near linear but shows a weak dependence on metallicity and UV field strength. N is approximately 1 in the G.10 models, but in the G.01 models, we find a steeper slope of $N \sim 1.2$.

DATA AVAILABILITY STATEMENT

All data are available upon request by the authors of this work.

REFERENCES

Bate M. R., Bonnell I. A., Price N. M., 1995, MNRAS, 277, 362
Bigiel F., Leroy A., Walter F., Brinks E., de Blok W. J. G., Madore B., Thornley M. D., 2008, AJ, 136, 2846
Bolatto A. D., Wolfire M., Leroy A. K., 2013, ARA&A, 51, 207
Bubel A.-P., 2015, Master's thesis, Ruprecht-Karls-Universität Heidelberg
Chevance M. et al., 2022, MNRAS, 509, 272
Clark P. C., Glover S. C. O., Klessen R. S., 2012, MNRAS, 420, 745
Clark P. C., Glover S. C. O., Ragan S. E., Duarte-Cabral A., 2019, MNRAS, 486, 4622
Crnojević D. et al., 2014, MNRAS, 445, 3862
Dale J. E., Ngoumou J., Ercolano B., Bonnell I. A., 2014, MNRAS, 442, 694
Dashyan G., Dubois Y., 2020, A&A, 638, A123
de los Reyes M. A. C., Kennicutt R. C. J., 2019, ApJ, 872, 16
Evans Neal J. I. et al., 2009, ApJS, 181, 321
Evans Neal J. I., Heiderman A., Vutisalchavakul N., 2014, ApJ, 782, 114
Federrath C., Banerjee R., Clark P. C., Klessen R. S., 2010, ApJ, 713, 269
Federrath C., Sur S., Schleicher D. R. G., Banerjee R., Klessen R. S., 2011, ApJ, 731, 62

Filho M. E., Sánchez Almeida J., Amorín R., Muñoz-Tuñón C., Elmegreen B. G., Elmegreen D. M., 2016, ApJ, 820, 109

Gatto A. et al., 2017, MNRAS, 466, 1903

Gil de Paz A. et al., 2007, ApJS, 173, 185

Glover S. C. O., Clark P. C., 2012a, MNRAS, 421, 116

Glover S. C. O., Clark P. C., 2012b, MNRAS, 426, 377

Gong M., Ostriker E. C., Wolfire M. G., 2017, ApJ, 843, 38 (GOW17)

Hamedani Golshan R., Javadi A., van Loon J. T., Khosroshahi H., Saremi E., 2017, MNRAS, 466, 1764

Harris J., Zaritsky D., 2004, AJ, 127, 1531

Harris J., Zaritsky D., 2009, AJ, 138, 1243

Helfer T. T., Thornley M. D., Regan M. W., Wong T., Sheth K., Vogel S. N., Blitz L., Bock D. C. J., 2003, ApJS, 145, 259

Hernquist L., 1990, ApJ, 356, 359

Heyer M., Gutermuth R., Urquhart J. S., Csengeri T., Wienen M., Leurini S., Menten K., Wyrowski F., 2016, A&A, 588, A29

Hopkins P. F., Kereš D., Oñorbe J., Faucher-Giguère C.-A., Quataert E., Murray N., Bullock J. S., 2014, MNRAS, 445, 581

Hu C.-Y., Naab T., Walch S., Glover S. C. O., Clark P. C., 2016, MNRAS, 458, 3528

Hu C.-Y., Naab T., Glover S. C. O., Walch S., Clark P. C., 2017, MNRAS, 471, 2151

Hu C.-Y., Sternberg A., van Dishoeck E. F., 2021, ApJ, 920, 44

Hunter J. D., 2007, Comput. Sci. Eng., 9, 90

Hunter G. H., Clark P. C., Glover S. C. O., Klessen R. S., 2021, preprint (arXiv:2109.06195)

Inutsuka S.-i., Inoue T., Iwasaki K., Hosokawa T., 2015, A&A, 580, A49

James B. L., Kumari N., Emerick A., Koposov S. E., McQuinn K. B. W., Stark D. P., Belokurov V., Maiolino R., 2020, MNRAS, 495, 2564

Jeffreson S. M. R., Kruijssen J. M. D., 2018, MNRAS, 476, 3688

Jeffreson S. M. R., Krumholz M. R., Fujimoto Y., Armillotta L., Keller B. W., Chevance M., Kruijssen J. M. D., 2021, MNRAS, 505, 3470

Joshi P. R., Walch S., Seifried D., Glover S. C. O., Clarke S. D., Weis M., 2019, MNRAS, 484, 1735

Kennicutt R. C., Evans N. J., 2012, ARA&A, 50, 531

Kennicutt R. C. J. et al., 2003, PASP, 115, 928

Kim C.-G., Ostriker E. C., 2017, ApJ, 846, 133

Kimm T., Cen R., 2014, ApJ, 788, 121

Kruijssen J. M. D., Longmore S. N., 2014, MNRAS, 439, 3239

Krumholz M. R., 2012, ApJ, 759, 9

Krumholz M. R., McKee C. F., 2005, ApJ, 630, 250

Krumholz M. R., Dekel A., McKee C. F., 2012, ApJ, 745, 69

Leroy A. K., Walter F., Brinks E., Bigiel F., de Blok W. J. G., Madore B., Thornley M. D., 2008, AJ, 136, 2782

Maeder A., 2009, Physics, Formation and Evolution of Rotating Stars. Springer, Berlin Heidelberg

Ness M., Freeman K., 2016, PASA, 33, e022

Olsen K. P. et al., 2021, ApJ, 922, 88

Omukai K., Hosokawa T., Yoshida N., 2010, ApJ, 722, 1793

Ostriker E. C., McKee C. F., Leroy A. K., 2010, ApJ, 721, 975

Pakmor R., Springel V., Bauer A., Mocz P., Munoz D. J., Ohlmann S. T., Schaal K., Zhu C., 2016, MNRAS, 455, 1134

Palla F., Salpeter E. E., Stahler S. W., 1983, ApJ, 271, 632

Pessa I. et al., 2021, A&A, 650, A134

Rafikov R. R., 2001, MNRAS, 323, 445

Rahman N. et al., 2012, ApJ, 745, 183

Rahner D., Pellegrini E. W., Glover S. C. O., Klessen R. S., 2019, MNRAS, 483, 2547

Rémy-Ruyer A. et al., 2014, A&A, 563, A31

Rezaeikh S., Javadi A., Khosroshahi H., van Loon J. T., 2014, MNRAS, 445, 2214

Roychowdhury S., Huang M.-L., Kauffmann G., Wang J., Chengalur J. N., 2015, MNRAS, 449, 3700

Shetty R., Kelly B. C., Rahman N., Bigiel F., Bolatto A. D., Clark P. C., Klessen R. S., Konstandin L. K., 2014, MNRAS, 437, L61

Shi Y., Armus L., Helou G., Stierwalt S., Gao Y., Wang J., Zhang Z.-Y., Gu Q., 2014, Nature, 514, 335

Simpson C. M., Bryan G. L., Hummels C., Ostriker J. P., 2015, ApJ, 809, 69

Sormani M. C., Treß R. G., Klessen R. S., Glover S. C. O., 2017, MNRAS, 466, 407

Springel V., 2005, MNRAS, 364, 1105

Springel V., 2010, MNRAS, 401, 791

Springel V., Di Matteo T., Hernquist L., 2005, MNRAS, 361, 776

Tress R. G., Smith R. J., Sormani M. C., Glover S. C. O., Klessen R. S., Mac Low M.-M., Clark P. C., 2020, MNRAS, 492, 2973

Truelove J. K., Klein R. I., McKee C. F., Holliman J. H. I., Howell L. H., Greenough J. A., 1997, ApJ, 489, L179

van der Walt S., Colbert S. C., Varoquaux G., 2011, Comput. Sci. Eng., 13, 22

Virtanen P. et al., 2020, Nat. Meth., 17, 261

Walch S. et al., 2015, MNRAS, 454, 238

Walter F., Brinks E., de Blok W. J. G., Bigiel F., Kennicutt R. C. J., Thornley M. D., Leroy A., 2008, AJ, 136, 2563

Weinberger R., Springel V., Pakmor R., 2019, ApJS, 248, 32

APPENDIX A: INFLUENCE OF BIN SIZE ON THE KENNICUTT–SCHMIDT RELATIONSHIP

Here, we examine the effects of changing the bin size on the KS relationship that we recover from our simulations. Kruijssen & Longmore (2014) show that a spatial scale of $\sim (500 \text{ pc})^2$ is a good compromise for measuring galactic star formation laws. On smaller scales, the relationship breaks down, and moving to larger scales detail is lost by averaging (particularly for a dwarf galaxy). However, different studies do use different apertures. For example, the Bigiel et al. (2008) results are based off a $(750 \text{ pc})^2$ aperture, while Pessa et al. (2021) use a range of resolutions from 100 pc to 1 kpc. We run a comparison on the KS relationship by increasing our bin size to $(1 \text{ kpc})^2$ to see what effect this will have on our results.

Our findings are summarized in Table A1. When we increase the bin size, the KS relation steepens, regardless of whether we consider H_2 or cold gas, becoming highly super-linear in all models. As before, decreasing the metallicity steepens both slopes, but the impact of varying the UV field strength is more mixed: decreasing it steepens the slope of both relationships in the $0.10 \, Z_\odot$ simulations but has no impact on N_{H_2} and actually decreases N_{COLD} in the $0.01 \, Z_\odot$ simulations.

If we look at the depletion times for different column densities, we see the same trend as for the $(500 \text{ pc})^2$ bins (Figs 18 and 19), with shorter times at higher densities. We also see a downturn in the cold gas depletion time in the lowest cold gas surface density bin, but this appears to be due to the small mass of gas at these densities.

At spatial scales of 1 kpc^2, each bin covers nearly a quarter of the area of the galactic disc, and as we use square bins, this includes substantial diffuse gas from outside the disc. As a result of this, our KS relationship (for these models at this spatial scale, Fig. 20) cannot be considered an accurate representation of the true value. The results we obtain with a $(500 \text{pc})^2$ bin better follow the gas distribution and

Table A1. Power-law slopes (N) for the Kennicutt–Schmidt law for the four models based on Σ_{H_2} and Σ_{COLD} at 1-kpc resolution with standard errors from linear regression statistics. The KS slope is super-linear for all models with no correlation between models and H_2 and cold gas relations.

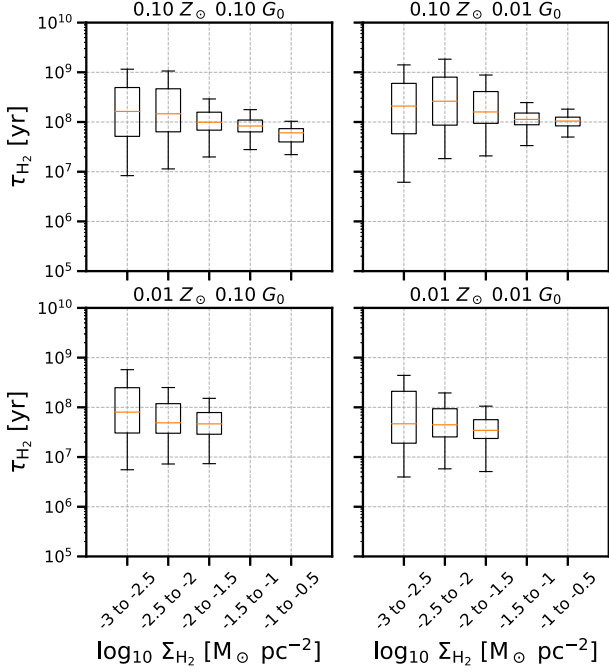|	N_{H_2} (1 kpc)	N_{COLD}
Z.10 G.10	1.16 ± 0.014	1.26 ± 0.015
Z.10 G.01	1.32 ± 0.012	1.51 ± 0.015
Z.01 G.10	1.45 ± 0.045	1.65 ± 0.044
Z.01 G.01	1.44 ± 0.046	1.59 ± 0.031

Figure 18. Local 1-kpc scale H_2 depletion times binned as a function of H_2 column density. In all models, we see a shorter depletion time in the dense H_2 with it rising in the more diffuse gas. We note that there are no $(1\,\mathrm{kpc})^2$ bins with mean H_2 surface densities greater than $10^{-2}\,M_\odot\,\mathrm{pc}^{-2}$ in the $0.01\,Z_\odot$ models.

Figure 19. Local 1-kpc scale cold gas depletion times binned as a function of cold gas column density. In all models, we see a shorter depletion time in the diffuse cold gas with it being fairly consistent across column densities.

therefore are more representative of the true KS relationship within our models.

Finally, to check whether the KS relationship is affected by time evolution, we measured the power-law indices for three different time periods in the steady state, taking data once again every Myr
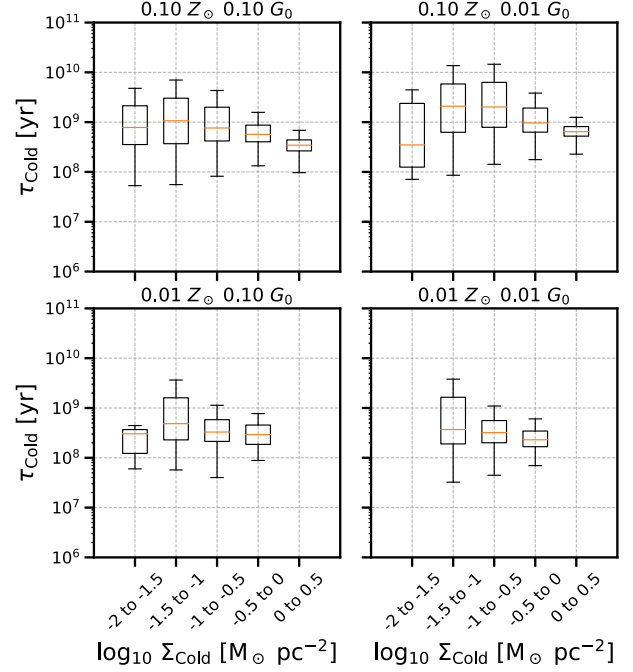
but only calculating the indices for periods of 100 Myr, 250 Myr, and 500 Myr instead of the entire 700-Myr steady-state period. The results can be seen in Table A2. We see small variations when taking data over different time periods but no evidence for large-scale time evolution.

Table A2. Power-law slopes (N) for the Kennicutt–Schmidt law for the four models based on Σ_{H_2} and Σ_{COLD} at 500-pc resolution with standard errors from linear regression statistics averaged over different time periods. The KS slope is mildly super-linear in almost all models with no correlation between models and H_2 and cold gas relations.

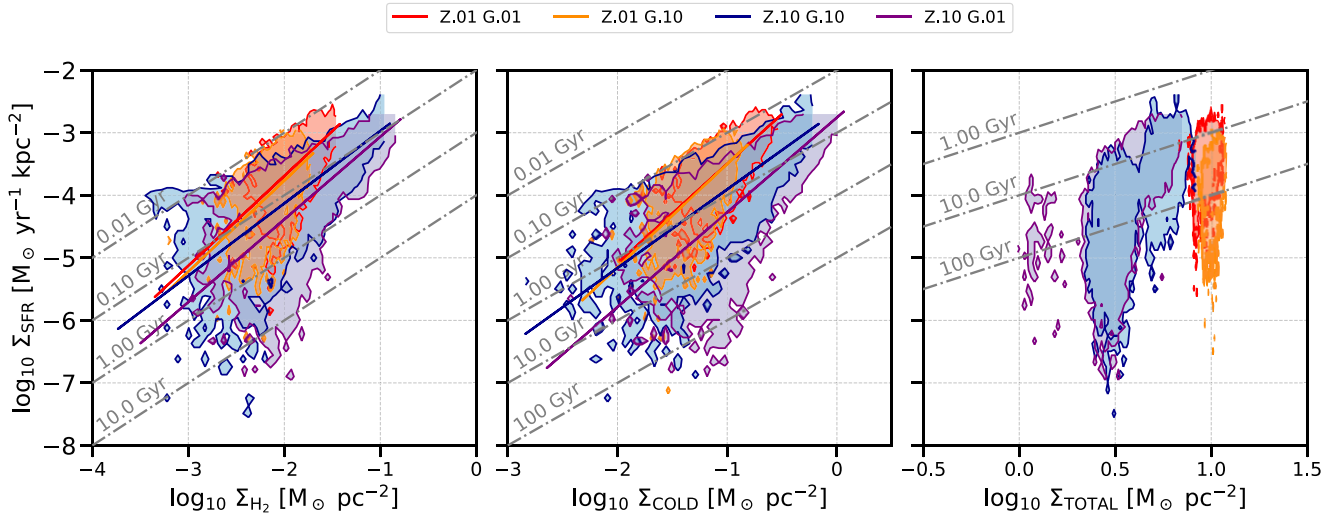|	N_{H_2} (100 Myr)	N_{COLD} (100 Myr)	N_{H_2} (250 Myr)	N_{COLD} (250 Myr)	N_{H_2} (500 Myr)	N_{COLD} (500 Myr)
Z.10 G.10	1.06 ± 0.037	1.19 ± 0.036	1.07 ± 0.025	1.13 ± 0.024	1.05 ± 0.017	1.12 ± 0.017
Z.10 G.01	1.17 ± 0.034	1.19 ± 0.034	1.18 ± 0.020	1.23 ± 0.021	1.17 ± 0.014	1.20 ± 0.014
Z.01 G.10	1.00 ± 0.066	1.25 ± 0.072	0.90 ± 0.046	1.18 ± 0.049	0.96 ± 0.030	1.21 ± 0.033
Z.01 G.01	1.25 ± 0.069	1.42 ± 0.099	1.19 ± 0.035	1.34 ± 0.034	1.25 ± 0.025	1.41 ± 0.024

Figure 20. Kennicutt–Schmidt relationship for the steady-state time period for each model, based on a 1-kpc bin. The legend is the same as the plot for the 500-pc bin. The relationships are steeper than in the 500-pc plot.

APPENDIX B: ACCOUNTING FOR MOLECULAR GAS IN SINK PARTICLES

In our star formation model, we assume that a fraction ϵ_{SF} of the gas accreted by sink particles goes on to form stars, with the remaining gas eventually being recycled to the ISM, as explained in Section 2.3. By default, we do not account for this gas when computing the molecular gas or cold gas masses, since we have no definite information regarding its chemical or thermal state. However, it is likely that some significant fraction of this gas is actually cold and molecular. Therefore, in this section, we examine how our results would change if we were to assume that all of this gas in sinks younger than 3 Myr[2] was cold and molecular, as in Olsen et al. (2021).

Accounting for this gas results in a slight (~50 per cent) increase in the H_2 depletion time, as summarized in Table B1 and Fig. 23. However, it still remains substantially smaller than both the cold gas depletion time and the characteristic depletion time of molecular gas in metal-rich spirals. We also find a small increase in the H_2 mass fraction, Fig 25, although in each case the gas is still very much HI-dominated.

The molecular KS relationship also flattens slightly when we include the contribution of the gas in the sinks to the molecular gas surface density, Table B2 and Fig 24. This behaviour is expected, since by making this change we are adding additional molecular gas predominantly to regions that have a large number of young sinks, i.e. regions with a high Σ_{SFR}. However, the change in N_{H_2} resulting from this is relatively small, ranging from approximately zero in run Z.10 G.01 to ~0.1 in run Z.01 G.01. Therefore, none of our results regarding the molecular KS relationship are strongly affected by this change. We also find that the cold gas KS relationship barely changes when we account for the cold gas in sinks, behaviour which is easy to understand if this is only a small fraction of the total amount of cold gas present in our simulated galaxies.

Table B1. H_2 mass fractions and depletion times that we obtain if we assume that all of the non-star-forming gas in sinks 3 Myr old or younger is fully molecular.

	M_{H_2} / M_{HI+H_2}	$\tau_{dep/ss}$ (yr)	$\sigma_{\tau_{dep/ss}}$
Z.10 G.10	0.34%	1.39×10^8	4.53×10^7
Z.10 G.01	0.75%	1.67×10^8	4.07×10^7
Z.01 G.10	0.06%	7.88×10^7	2.14×10^8
Z.01 G.01	0.14%	6.11×10^7	7.77×10^7

Table B2. Power-law slopes (N) for the Kennicutt–Schmidt law for the four models based on Σ_{H_2} and Σ_{COLD} for a 500-pc bin when we account for the contribution made by molecular gas locked up in young sink particles. We recover slightly smaller values of N_{H_2} compared to the case where we neglect this gas, but N_{COLD} is barely affected.

	$N_{H_2+sinks}$	$N_{COLD + sinks}$
Z.10 G.10	1.06 ± 0.014	1.15 ± 0.014
Z.10 G.01	1.18 ± 0.011	1.23 ± 0.012
Z.01 G.10	0.88 ± 0.022	1.20 ± 0.028
Z.01 G.01	1.14 ± 0.018	1.41 ± 0.020

Finally, we show in Figs 21 and 22 how the H_2 and cold gas depletion times vary as a function of the corresponding surface density in the case where we account for the gas locked up in sinks. Comparing these with Figs 16 and 17, we see that there is little difference, and hence that our decision in the main text to neglect this gas has little impact on our results.

Given that the inclusion of molecular gas from young sink particles makes the KS relation shallower, rather than steeper, the results in the main portion of the paper can be considered as an upper limit on the steepness of the KS slope with a 500-pc bin. A more detailed sink particle model and analysis would be needed to find the lower limit on the steepness of the KS slope.
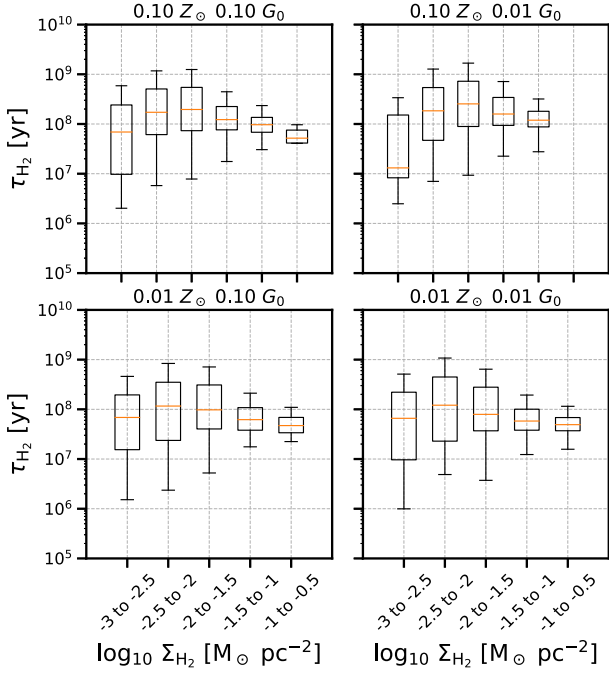
---

[2]We do not consider sinks older than 3 Myr as molecular gas associated with star-forming regions will frequently have been photodissociated or otherwise dispersed by this time; see e.g. Chevance et al. (2022).

Figure 21. Local 500-pc scale H₂ depletion times with sinks included binned as a function of H₂ column density. In all models, we see a shorter depletion time in the dense H₂ and an increase in the more diffuse gas.
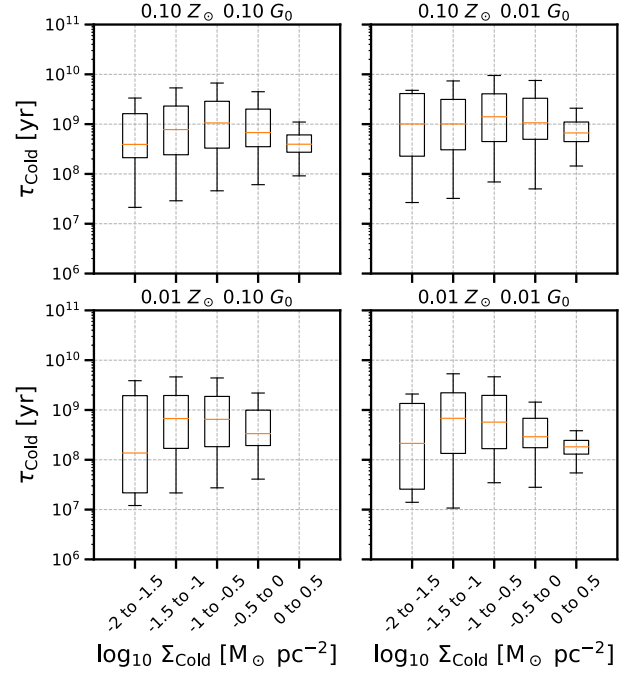
Figure 22. Local 500-pc scale cold gas depletion times with sinks included binned as a function of cold gas column density. In all models, we see a shorter depletion time in the diffuse cold gas with it being fairly consistent across column densities.
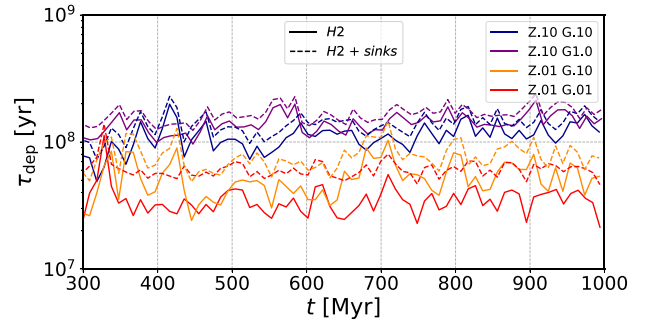

Figure 23. Time evolution of the average H₂ depletion time when we account for the molecular gas locked up in sinks with ages ≤3 Myr (dashed line) and when we do not (solid line). The inclusion of this gas slightly lengths the depletion time in each case.
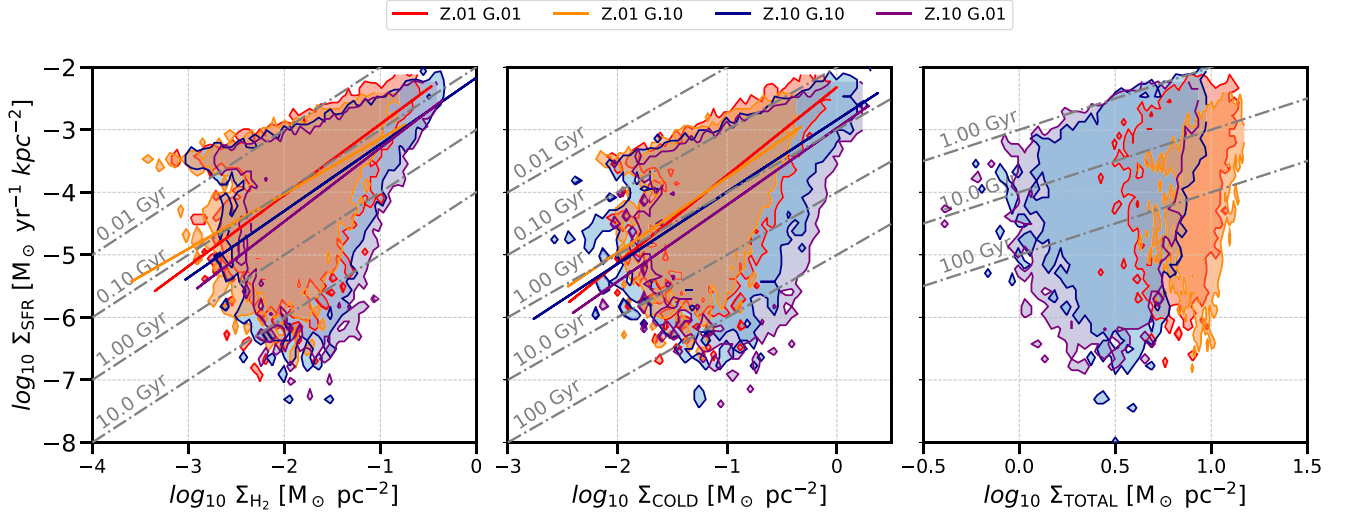
Figure 24. Kennicutt–Schmidt relationship for the steady-state time period for each model, based on a 500-pc bin and including the contribution to the H_2 surface density made by the molecular gas locked up in young (<3 Myr) sink particles. We see that the inclusion of this gas does not significantly affect the relationship that we recover.
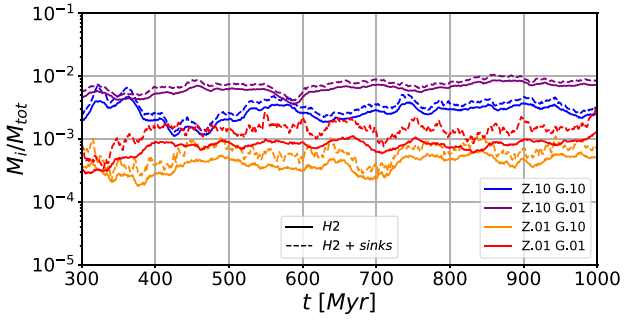
Figure 25. As Fig. 23, but for the H_2 mass fraction. There is a small increase in the mass fraction when we include the contribution from the sinks.

This paper has been typeset from a TEX/LATEX file prepared by the author.